UNIVERSITEIT LEIDEN

Quadrant Detector Response of Non-integer Orbital Angular Momentum Laser Beams

by

W.G. Stam

supervised by

Dr. A.M. Nugrowati

Prof.dr. J.P. Woerdman

in the

Faculteit der Wis- en Natuurwetenschappen

Opleiding Natuurkunde

August 2012

Abstract

In this report we have generated structurally propagation invariant laser beams carrying non-integer orbital angular momentum (OAM) using Hermite-Laguerre-Gaussian (HLG) modes. Secondly, calibration techniques have been discussed for beam positional measurements of these laser beams with a quadrant detector (QD). We have demonstrated, both analytically and experimentally, that the response of the quadrant detector is non-linear and highly dependent on the *orientation of the symmetry-axes* of the non-integer orbital angular momentum beam, as well as the, seperate, Hermite-Laguerre-Gaussian *mode orientation*. This mode orientation is an indication of the orbital angular momentum content of the laser beam. From these response profiles of each of the orientations of the HLG mode we have calculated the calibration constant of and the location in the beam intensity pattern for which the quadrant detector is most sensitive for measuring beam displacement. This location, as confirmed by our experiment is typically not in the beam center.

Contents

Abstract i

Abbreviations iv

1 Introduction 1

2 Hermite-Laguerre-Gaussian Mode Generation and Characterization 4
- 2.1 Theory of Higher Order Gaussian modes . . . 4
  - 2.1.1 Hermite-Gaussian and Laguerre-Gaussian modes . . . 4
  - 2.1.2 Astigmatic Mode Converters . . . 7
  - 2.1.3 Hermite-Laguerre-Gaussian modes . . . 8
- 2.2 Method . . . 10
- 2.3 Intensity characterization . . . 11
  - 2.3.1 Experimental Setup . . . 11
  - 2.3.2 Results . . . 13
- 2.4 Phase characterization . . . 14
  - 2.4.1 Experimental Setup . . . 14
  - 2.4.2 Results . . . 15
- 2.5 Discussion . . . 17

3 Positional Measurements Using Quadrant Detectors 18
- 3.1 Theory of Quadrant Qetector Response . . . 18
  - 3.1.1 Quadrant Detector Response . . . 18
  - 3.1.2 Rotation of symmetry axes . . . 20
  - 3.1.3 Linearity and Calibration Constant . . . 21
- 3.2 Method . . . 23
- 3.3 Experimental setup . . . 24
- 3.4 Results . . . 25
  - 3.4.1 Position-current relation . . . 25
  - 3.4.2 Calibration Constant . . . 27
- 3.5 Discussion . . . 29

4 Conclusion 30

A Matlab Simulation Codes 31

A.1 HG mode simulation 31
A.2 LG mode simulation 32
A.3 HLG mode simulation 33
A.4 plane wave simulation 34

B A.M. Nugrowati, W.G. Stam, J.P. Woerdman, "Position measurement of non-integer OAM beams with structurally invariant propagation" 35

Bibliography 48

Abbreviations

QD	**Q**uadrant **D**etector
OAM	**O**rbital **A**ngular **M**omentum
LG	**L**aguerre **G**aussian
HG	**H**ermite **G**aussian
HLG	**H**ermite **L**aguerre **G**aussian
CCD	**C**harged **C**oupled **D**evice

Chapter 1

Introduction

Recently there has been a lot of interest in orbital angular momentum (OAM) laser beams that operate in Laguerre-Gaussian (LG) modes. The Laguerre-Gaussian modes have a doughnut shaped intensity pattern and carry orbital angular momentum due to their helical wavefront shape[1, 2]. Everytime we make a round trip about the propagation axis we gain $2\pi l$ phase, with l the azimuthal mode index of the Laguerre-Gaussian mode, which indicates an *integer* orbital angular momentum value of $l\hbar$ per photon. Great attention has been given to beams carrying *integer* orbital angular momentum which is reflected by the range of research connected to these laser beams. From optical tweezers[3, 4] to quantum communication[5, 6] and from stellar detection[7, 8] to nanometer precision metrology on beam shifts[9].

We can also derive intermediate forms of Laguerre-Gaussian and Hermite-Gaussian (HG) modes that retain many of the properties of these two families of Gaussian beams. These modes are called Hermite-Laguerre-Gaussian (HLG) modes and in these intermediate modes we can speak of *non-integer* orbital angular momentum[10, 11, 12]. *Non-integer* orbital angular momentum means that when we rotate about the propagation axis we will not gain a phase of 2π times an integer l, but 2π times a non-integer l. These Hermite-Laguerre-Gaussian modes, due to their non-integer values of their orbital angular momentum, potentially broaden the applicability of orbital angular momentum beams. This is most insightful when we take the example of applying orbital angular momentum beams for optical trapping. If we take a Laguerre-Gaussian mode with *integer* orbital angular momentum l the trapped particle experiences a rotational force

proportional to l. With Hermite-Laguerre-Gaussian modes we can tune this l continuously and therefore also tune the rotational force continuously.

There are various techniques for creating orbital angular momentum beams of which we shall mention three widely used methods. The first is the so-called astigmatic $\pi/2$-mode converter[13] which applies a Gouy phase difference between the components of a Hermite-Gaussian mode to create a well defined Laguerre-Gaussian mode with an integer orbital angular momentum. The second method is done with a spiral phase plate[14, 15, 16] and the third method being computer generated holograms[3, 17]. Both the spiral phase plate and the computer generated holograms do not convert an incoming Gaussian mode into pure Laguerre-Gaussian modes, but rather into a superposition of Laguerre-Gaussian modes with different radial mode indices. Therefore, we have chosen, and we will discuss this further in the report, the astigmatic mode converter because it has the advantage that it creates propagationally invariant, and pure, Laguerre-Gaussian modes, as compared to the other two methods. This method also allows for tuning the mode converter such that it creates a Hermite-Laguerre-Gaussian mode carrying non-integer orbital angular momentum[18].

Accurate beam positional measurement is crucial for many of the applications of beams carrying non-integer orbital angular momentum. A popular and very sensitive device for beam positional measurement is a quadrant detector (QD). A quadrant detector is two by two array of photodiodes that measures the total intensity on each of the quadrants. Due to the finite number of pixels (only four!) used in a measurement with a quadrant detector, a sufficient characterisation is required of the intensity pattern of the beam that is to be measured. The quadrant detector response is non-trivial for non-integer orbital angular momentum beams and many studies have been carried out for the fundamental Gaussian mode[19, 20, 21] and recently for beams carrying integer orbital angular momentum[22]. In this report we will present a general calibration technique for positional measurements of non-integer orbital angular momentum beams with a quadrant detector.

The goal of this research is twofold. The first goal is to generate and characterize the laser beams operating in Hermite-Laguerre-Gaussian modes carrying non-integer

orbital angular momentum. The second goal is to characterize the quadrant detector response to the non-integer orbital angular momentum beams. These characterizations can then be used in calibrating the quadrant detector response to accurately measure positional shifts for these type of beams.

The topic of generating and characterizing Hermite-Laguerre-Gaussian modes is adressed in chapter two and the quadrant detector response along with the calibration technique is adressed in chapter three. Each chapter is structured by the following paragraphs: theory, method, experimental setup, results and discussion. Chapter four concludes the report. The appendices give some additional information. Appendix A shows the Matlab codes used to produce the simulations shown in the results. Appendix B is a paper, that is partly based on the work of this thesis.

Chapter 2

Hermite-Laguerre-Gaussian Mode Generation and Characterization

2.1 Theory of Higher Order Gaussian modes

2.1.1 Hermite-Gaussian and Laguerre-Gaussian modes

In the paraxial approximation the wave equation, governing the static electromagnetic field distribution in the resonating laser cavity, takes the following form[23, 24]:

$$\frac{\partial^2}{\partial x^2}u(x,y,z,) + \frac{\partial^2}{\partial y^2}u(x,y,z,) - 2ik\frac{\partial}{\partial z}u(x,y,z,) = 0 \ , \tag{2.1}$$

where $k = 2\pi/\lambda$ is the wavenumber and $U(x,y,z) = u(x,y,z,)\exp(-ikz)$ the electric field distribution. A solution to the paraxial wave equation, also called the fundamental Gaussian mode, is readily found to be:

$$u^G(x,y,z) = \sqrt{\frac{2}{\pi}}\frac{1}{w(z)}e^{i(\frac{-k(x^2+y^2)}{2R(z)}+\Psi(z))}e^{\frac{-(x^2+y^2)}{w(z)^2}} \ . \tag{2.2}$$

This solution represents a propagating wave in the z-direction with a Gaussian intensity pattern. Its beam parameters are depicted in figure 2.1. It has curved wavefronts of radius $R(z) = (z^2 + z_R^2)/z$ and a beam radius, or spot size, $w(z)^2 = w_0^2(1 + z^2/z_R^2)$. The parameter $z_R = (\pi w_0^2)/\lambda$ is the so called Rayleigh range, an indication for the distance along the propagation axis from the waist to the place where the area of the cross section

is doubled. This means that if we move along the z-axis from the waist with a distance z_R the beam waist increases by a factor of $\sqrt{2}$. Also the radius of curvature changes from $R = \infty$ at $z = 0$ to $R \approx z$ for $z \gg z_R$. The Gouy phase $\Psi(z) = \arctan(z/z_R)$ indicates the phase shift of π as the beam passes through its waist, in addition to the normal change in phase as the beam propagates. We now seek a general Gaussian

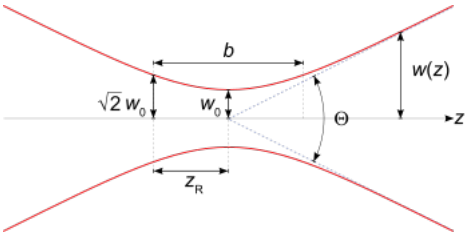

FIGURE 2.1: Beam parameters of a Gaussian beam. This figure has been taken from Ref. [25]

solution of the paraxial wave equation for an arbitrary amplitude distribution in a given xy-plane. In Cartesian coordinates a complete and orthogonal set of solutions is given by the Hermite-Gaussian (HG) modes, which can be expressed analytically:

$$u^{HG}_{n,m}(x,y,z) = \frac{C^{HG}_{nm}}{w(z)} e^{i(\frac{-k(x^2+y^2)}{2R(z)} + (n+m+1)\Psi(z))} e^{\frac{-(x^2+y^2)}{w(z)^2}} H_n(\frac{x\sqrt{2}}{w(z)}) H_m(\frac{y\sqrt{2}}{w(z)}) \ , \qquad (2.3)$$

with n, m mode indices, $C^{HG}_{nm} = \sqrt{2/(\pi n! m!)} 2^{-\frac{1}{2}(n+m)}$ a normalization constant and $H_n(x)$ Hermite polynomials. In cylindrical coordinates another complete and orthogonal set of solutions is given by the Laguerre-Gaussian (LG) modes, which can be expressed analytically:

$$\begin{aligned} u^{LG}_{n,m}(r,\phi,z) \quad = \quad & \frac{C^{LG}_{nm}}{w(z)} (-1)^{min(n,m)} (\frac{r\sqrt{2}}{w(z)})^{|n-m|} e^{i(\frac{-kr^2}{2R(z)} + (n+m+1)\Psi(z))} \\ & \cdot e^{\frac{-r^2}{w(z)^2}} e^{-i(n-m)\phi} L^{|n-m|}_{min(m,n)}(\frac{2r^2}{w^2(z)}) \ , \end{aligned} \qquad (2.4)$$

with n, m mode indices, another normalization constant $C^{LG}_{nm} = min(m,n)\sqrt{2/(\pi n! m!)}$ and $L^l_p(x)$ generalized Laguerre polynomials. Note that we have written mode indices n, m instead of the normal p, l mode-indices (these indices can be related with $p = min(m,n), l = n - m$), which is useful in our following discussion of mode conversion. If we neglect the z-dependent phase factors and take the spot size to be unity, at a given

xy-plane the distribution of the electric field can be written as:

$$u^{HG}_{n,m}(x,y) = C^{HG}_{nm} e^{-(x^2+y^2)} H_n(x\sqrt{2}) H_m(y\sqrt{2}) \ , \tag{2.5}$$

$$u^{LG}_{n,m}(r,\phi) = C^{LG}_{nm} e^{-r^2} (-1)^{min(n,m)} (r\sqrt{2})^{|n-m|} e^{-i(n-m)\phi} L^{|n-m|}_{min(n,m)}(2r^2) \ . \tag{2.6}$$

The first few orders of $u^{HG}_{n,m}$ and $u^{LG}_{n,m}$ modes are shown in figure 2.2 and are listed analytically below:

$$\begin{aligned}
u^{HG}_{00}(x,y) &= \sqrt{\tfrac{2}{\pi}}\, e^{-(x^2+y^2)} \ , & u^{LG}_{00}(r,\phi) &= \sqrt{\tfrac{2}{\pi}}\, e^{-r^2} \ , \\
u^{HG}_{10}(x,y) &= \sqrt{\tfrac{8}{\pi}}\, x\, e^{-(x^2+y^2)} \ , & u^{LG}_{10}(r,\phi) &= \tfrac{4}{\sqrt{\pi}}(r^3 - r)\, e^{-r^2}\, e^{-i\phi} \ , \\
u^{HG}_{01}(x,y) &= \sqrt{\tfrac{8}{\pi}}\, y\, e^{-(x^2+y^2)} \ , & u^{LG}_{01}(r,\phi) &= \tfrac{4}{\sqrt{\pi}}(r^3 - r)\, e^{-r^2}\, e^{i\phi} \ , \\
u^{HG}_{11}(x,y) &= \tfrac{8}{\sqrt{\pi}}\, xy\, e^{-(x^2+y^2)} \ , & u^{LG}_{11}(r,\phi) &= \sqrt{\tfrac{2}{\pi}}(2r^2 - 1)\, e^{-r^2} \ , \\
u^{HG}_{20}(x,y) &= \tfrac{4x^2-1}{\sqrt{\pi}}\, e^{-(x^2+y^2)} \ , & u^{LG}_{20}(r,\phi) &= \tfrac{8r^2}{\sqrt{\pi}}(r^4 - 4r^2 + 3\, e^{-r^2}\, e^{-2i\phi} \ .
\end{aligned}$$

Important to note is that both their zero order modes reduce to the fundamental Gaussian mode $\exp(-x^2-y^2)$ and that their intensities and phase distributions do not change upon propagation. The HG modes are always a Gaussian exponential combined with some polynomial in x and y of order $n+m$. The LG modes carry integer orbital angular momentum (OAM) $l = n-m$ as can be seen by the azimuthal dependent phase exponential $\exp(-i(n-m)\phi)$. The phase increases linearly if we rotate about the propagation axis to a total of $2\pi l$ in a full rotation, as illustrated in the third picture of figure 2.4.

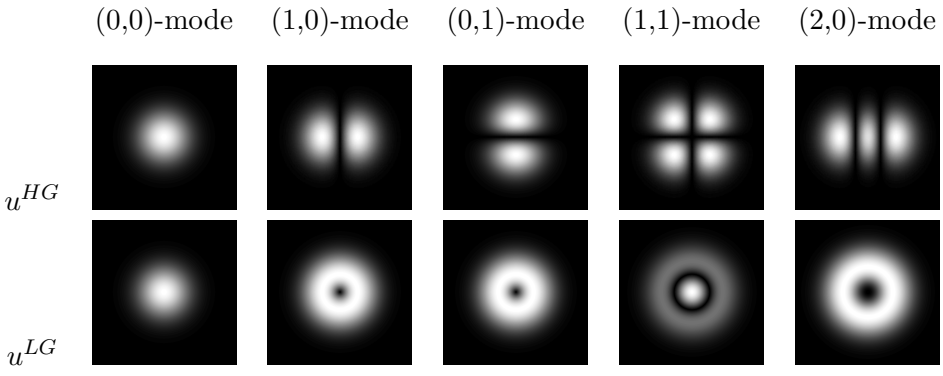

FIGURE 2.2: Example of the intensity distributions of the lower order HG and LG (n,m)-modes. The intensity distributions of the HG and LG modes are rectangularly and cylindrically symmetric respectively.

We can also relate the HG and LG modes analytically and therefore decompose the LG modes into HG modes and vice versa. This has been shown in Ref. [10, 13] by using

relations between the Laguerre and Hermite polynomials and in Ref. [11] by operator algebra. Their results are denoted in the following expression for a decompostion of LG modes into HG modes:

$$u_{n,m}^{LG} = \sum_{\kappa=0}^{n+m} i^{\kappa} b(n,m,\kappa) u_{N-\kappa,\kappa}^{HG} \ , \tag{2.7}$$

with coefficients

$$b(n,m,\kappa) = \sqrt{\frac{(n+m-\kappa)!\kappa!}{2^{n+m}n!m!}} \cdot \frac{1}{\kappa!}\frac{d^{\kappa}}{dt^{\kappa}}\left[(1-t)^{n}(1+t)^{m}\right]_{t=0} \ . \tag{2.8}$$

The factor i^{κ} indicates a $\pi/2$ phase difference between successive components of the decomposition of a LG mode into a HG mode. Important to note is that, while it is trivial that any HG mode with arbitrary principal axes can be projected onto, or decomposed into, two HG modes with orthogonal principal axes, a diagonal HG mode (i.e. HG modes whose principal axes are rotated by 45° with respect to the orthogonal reference principal axes), can be decomposed into the exact same set as the LG mode, but with the successive components in phase. This is seen in the resemblance between equation (2.7) and the following equation:

$$u_{n,m}^{HG}\left(\frac{x+y}{\sqrt{2}}, \frac{x-y}{\sqrt{2}}\right) = \sum_{\kappa=0}^{n+m} b(n,m,\kappa) u_{N-\kappa,\kappa}^{HG} \ . \tag{2.9}$$

This gives us direct means to convert a HG mode into a LG mode by giving the projection onto the y-axis of a diagonal mode a phase shift of $\pi/2$ compared to its projection onto the x-axis, as will be discussed in the next paragraph.

2.1.2 Astigmatic Mode Converters

In order to convert a HG mode into a LG mode we need to introduce a difference in the phase between the two orthogonal components of a diagonal HG mode. Such a difference in phase between two orthogonal components can be achieved by the Gouy phase, i.e. the phase a Gaussian beam gains when going through the beam waist. In an astigmatic beam there is a difference between the Rayleigh ranges z_{Rx} and z_{Ry} of the orthogonal components and thus also a difference between the components in the total Gouy phase. If we introduce astigmatism in a confined region by means of two

cylindrical lenses positioned a distance d apart, such that the two transverse radii of the astigmatic beam are equal to the radius of curvature of the lens, there will be a total phase difference ψ between the two components due to the Gouy phase. See also figure 2.3. For a pure conversion between HG and LG modes we set $\psi = \pi/2$. This is achieved if the distance between the cylindrical lenses is:

$$d = f\sqrt{2}\ , \tag{2.10}$$

with f the focal length of the cylindrical lenses, and the input beam has a Rayleigh range:

$$z_R = f + \frac{d}{2} = (1 + \frac{1}{2}\sqrt{2})f\ . \tag{2.11}$$

A diagonal HG mode traversing a $\pi/2$-mode converter receives a factor i^κ between the succesive components of equation (2.7) and is thus converted into a LG mode. If a LG mode traverses through the same configuration the output is of course by symmetry a conversion into a diagonal HG mode.

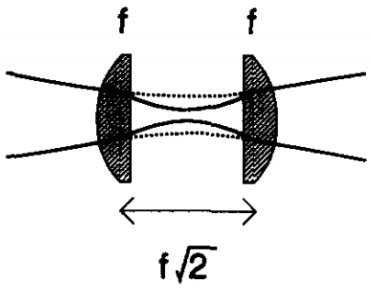

FIGURE 2.3: Modematched cylindrical lenses for $\psi = \pi/2$. The dashed lines indicate the unfocused transverse direction and the solid lines indicate the focused transverse direction. This figure is taken from Ref. [1]

2.1.3 Hermite-Laguerre-Gaussian modes

For a HG mode with principle axes rotated by an arbitrary angle α with respect to the $\pi/2$-mode converter the output beam is neither in a LG nor in a HG mode but can be described as an analytical interpolation between these modes. We call these modes Hermite-Laguerre-Gaussian (HLG) modes. The HLG modes as a function of α

are described analytically as[1]:

$$\begin{aligned} u^{HLG}_{n,m}(x,y|\alpha) &= C^{HLG}_{nm} e^{-(x^2+y^2)} \sum_{\kappa=0}^{n+m} i^{\kappa} \cos^{n-\kappa}\alpha \sin^{m-\kappa}\alpha \\ &\quad \cdot P^{(n-\kappa,m-\kappa)}_{\kappa}(-\cos 2\alpha) H_{n+m-\kappa}(\sqrt{2}x) H_{\kappa}(\sqrt{2}y) \ , \end{aligned} \tag{2.12}$$

where $P^{(\beta_1,\beta_2)}_{\kappa}(x)$ are Jacobi polynomials and $C^{HLG}_{nm} = \sqrt{2/(\pi n!m!)}2^{-\frac{1}{2}(n+m)}$ another normalization constant. Note that the notation used is the same as for the introduction of Hermite-Laguerre-Gaussian modes in Ref. [10]. This result reduces to HG modes for $\alpha = N \cdot 90°$ and LG modes for $\alpha = 45° + N \cdot 90°$, where N is an integer, as expected. Intermediate HLG modes retain many of the features of HG and LG modes. Because they are an analytical interpolation between HG and LG modes they remain structurally propagational invariant, i.e. their phase and intensity distribution do not change upon propagation. All modes have a Gaussian component $\exp(-x^2-y^2)$ and some polynomial in x, y of degree $m+n$. The first order HLG modes described analytically as:

$$\begin{aligned} u^{HLG}_{0,0}(x,y|\alpha) &= e^{-x^2-y^2} \ , \\ u^{HLG}_{1,0}(x,y|\alpha) &= e^{-x^2-y^2} 2\sqrt{2}(x\cos\alpha + iy\sin\alpha) \ , \\ u^{HLG}_{0,1}(x,y|\alpha) &= e^{-x^2-y^2} 2\sqrt{2}(x\sin\alpha - iy\cos\alpha) \ , \\ u^{HLG}_{1,1}(x,y|\alpha) &= e^{-x^2-y^2}((4x^2+4y^2-2)\sin 2\alpha - 8ixy\cos 2\alpha) \ , \\ u^{HLG}_{2,0}(x,y|\alpha) &= e^{-x^2-y^2}(8(x\cos\alpha + iy\sin\alpha)^2 - 2\cos 2\alpha) \ . \end{aligned} \tag{2.13}$$

It follows that for a fixed α the HLG modes also constitute a complete orthogonal set of solutions for the paraxial wave equation. An important feature of the HLG modes is that the OAM takes values of:

$$l = (n-m)\sin(2\alpha) \ , \tag{2.14}$$

and that the phase shift is non-linear in the azimuthal direction. This can be visualized by looking at the phase distributions of the first order HG mode (phase of 0 and π in the respective lobes, with a phasestep between the lobes) and the first order LG mode (linear in the azimuthal angle ϕ). Consider now a HLG mode with $\alpha = 15°$. The phase profile still very much looks like a HG mode but the phase step has become vague and

[1] We take, as previously, $w(z) = 1$ and leave out the z-dependent phase terms

thus non-linear in the azimuthal direction as shown in figure 2.4. As we increase α to 45° the phase step slowly fades to a constant phase shift.

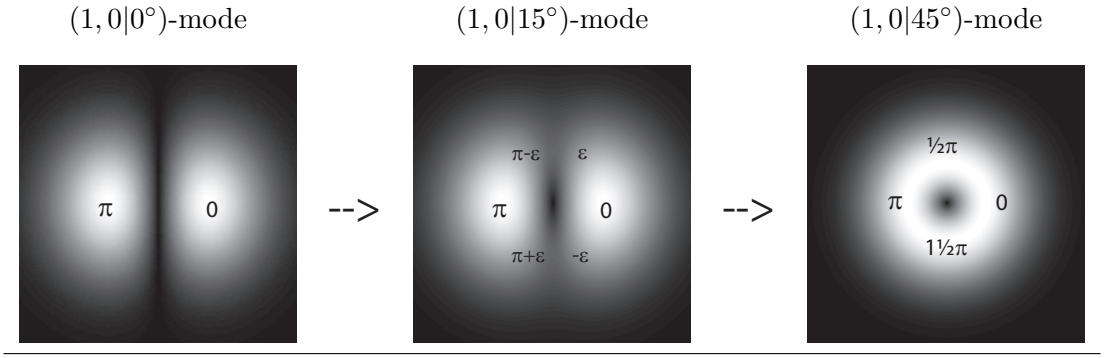

FIGURE 2.4: Slowly dissolving phase step when we change a HLG mode from a HG mode to a LG mode. The distribution is intensity and the numbers indicate the phase.

2.2 Method

The goal of this part of the research is to generate and characterize the HLG modes carrying non-integer OAM. The generation method will be, as described in the introduction, the conversion of HG modes using an astigmatic mode converter. The orientation α of the HG mode will determine the mode orientation of the HLG mode. Our laser produces HG modes up to order $(n, m) = (6, 6)$, but we force our laser to operate in a low order excited HG mode by inserting a thin wire perpendicular to the propagation axis, and subsequently blocking out the higher order terms by also inserting an aperture within the laser cavity. The wire forces the intensity to be zero at the position of the wire and therefore the laser cavity will resonate in the chosen HG mode. We can rotate the wire within the laser cavity and as such choose the orientation of our HG mode. Because the axes of our astigmatic mode converter are fixed in our setup the symmetry axes of the output HLG mode are also fixed; this highly simplifies the method for the quadrant detector calibration discussed in chapter 3. Our setup to generate HLG modes is depicted in figure 2.5. We have characterized the HLG modes by measuring their intensity profiles with a simple CCD device and by measuring their phase profiles by interfering a reference beam with our HLG mode. Such an interference pattern for LG modes shows the phase dislocation features as a pitchfork structure. For HG modes the interference pattern shows separated shifted lines as a result of the phase step between the lobes. In the case of HLG intermediate modes this pitchfork structure gradually dissolves into

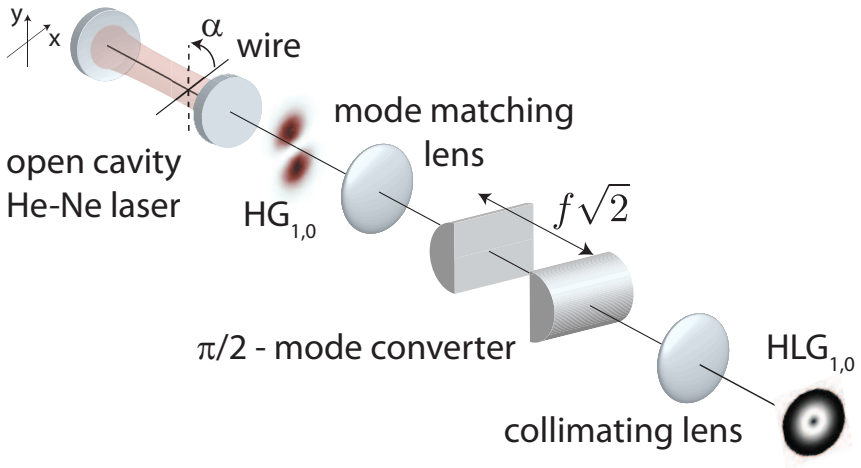

FIGURE 2.5: Experimental setup of HLG beam generation. A HG (1,0)-mode is generated in the open laser cavity with a angular tunable wire. The beam is guided through a mode matching lens, cylindrical lenses and a collimating lens to produce a HLG (1,0)-mode. The axes of the cylindrical lenses are fixed.

the shifted lines if we gradually change from LG to HG modes. We will limit our experimental work to the HLG (1,0)- and (2,0)-modes and in our measurements we have varied the angle α of the wire and thus the orientation of the HG mode between 0° and 90°. These orientations contain all the various possibilities of HLG modes because of the symmetrical properties of the HG modes. The only difference between a HG mode that is rotated by an angle of 180° is that the phase difference between the lobes is reversed. This translates to negative l-values if we create an HLG mode with α between 180° and 360°. Furthermore, in the range we have chosen the HLG mode is identical to the HLG mode in the range of 180° to 90°.

2.3 Intensity characterization

2.3.1 Experimental Setup

A HeNe gain tube operating at a wavelength of $\lambda = 632.8\,nm$ has been used throughout the experiments. The setup described in this paragraph is also shown in figure 2.6. The gain tube is placed between two spherical mirrors with radius of curvature $R_1 = 600\,mm$ and $R_2 = 750\,mm$ with a distance of $d_1 = 830\,mm$ between the mirrors. These parameters give a calculated beam waist of $w_0 = 241\,\mu m$. To force the gain tube to operate at a single higher order HG mode we use an aperture in combination with

a thin, 200 μm diameter wire. We choose the location of the aperture at 360 mm away from mirror R_2, such that we have control over blocking the higher order modes. We choose the location of the wire at 160 mm away from mirror R_2, which determines the required thickness of the wire. Our setup produces a beam in a HG mode with a total power of approximately 1 mW in the case of a (1,0)-mode and 0.6 mW in the case of a (2,0)-mode. Next in our setup is the mode converter, consisting of a mode matching lens

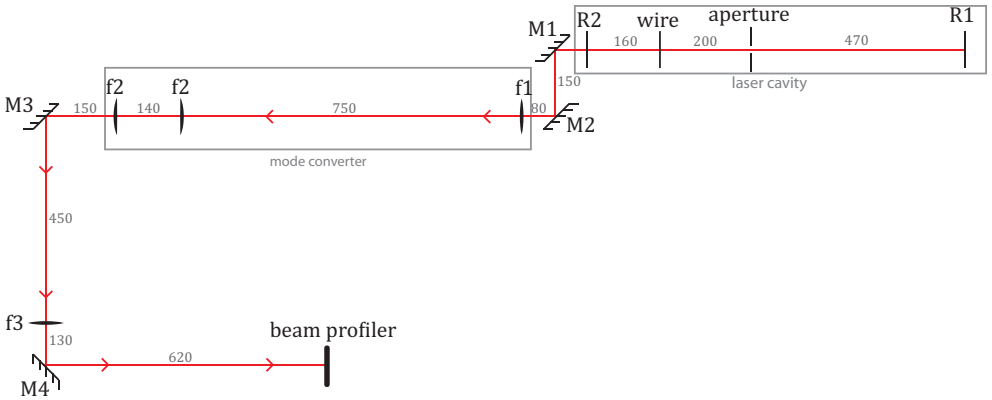

FIGURE 2.6: Experimental setup of HLG beam generation, topview. The figure shows the optical elements on the table as well as the distances between them in milimeters. The laser cavity is between the spherical mirrors R_1 and R_2. M_1 to M_4 are dielectric mirrors to guide the beam. From the laser cavity the beam is guided, by means of mirrors M_1 and M_2, through the mode matching lens with focal length f_1 and the cylindrical lenses with focal length f_2 as the mode converter. Further down the path is the collimating lens with focal length f_3 and finally at the end of the laser path is the CCD device, to characterize the beam profile.

of focal length $f_1 = 400\,mm$ and two cylindrical lenses of focal length $f_2 = 100\,mm$. The cylindrical lenses introduce the Gouy phase shift between the x and y component, and to obtain a $\pi/2$ Gouy phase shift, the position of the middle of these lenses with respect to the mode matching lens is $d_3 = 750\,mm$. The distances we have used for the mode matching lens is $d_2 = 300\,mm$ with respect to the laser cavity, and the distances between the two cylindrical lenses is according to equation (2.10) equal to: $d_4 = f_2\sqrt{2} = 140\,mm$.

To obtain the desired collimated beam for further measurement we implement a collimating lens, with focal length $f_3 = 500\,mm$ at $d_5 = 600\,mm$ away from the cylindrical lenses, producing a beam diameter of $w_2 = 545\,\mu m$. The obtained Rayleigh range of the collimated beam is: $z_{R,2} = \frac{\pi}{\lambda} w_2^2 = 1.5\,m$.

2.3.2 Results

We have measured the collimated HLG modes that are produced by the setup described in the previous paragraph with an CCD device, in particular with the Spiricon beam profiler, for the two lowest order excited HLG modes: the (1,0)-mode and the (2,0)-mode. The rotation angle α of the wire has been varied between 0° and 90° with steps of 15°. The analytical expression (2.13) of the HLG modes furthermore provides simulations[2] of the profile measurement. The results are displayed in figure 2.8. The four rows correspond to the (1,0)-mode beam profile measurement, (1,0)-mode beam profile simulation, the (2,0)-mode beam profile measurement and (2,0)-mode beam profile simulation, respectively.

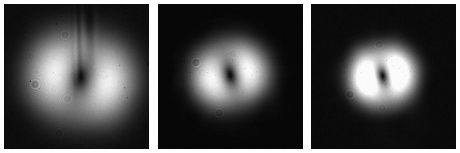

$\sim 0z_R$ $\sim 1z_R$ $\sim 2z_R$

FIGURE 2.7: Mode profiles at several Rayleigh distances z_R, representing the near- and far-field planes for the outgoing $u_{1,0}^{HLG}(x, y|30°)$ mode.

If we compare with figure 2.2 we see that for $\alpha = 0$ we obtain a HG (1,0)-mode, for $\alpha = 90°$ we obtain a HG (0,1)-mode and for $\alpha = 45°$ we obtain a LG (1,0)-mode. If we increase α from 0° to 90° the intermediate modes gradually change from the HG mode to the LG mode and back. The principal axes of the HLG mode remain fixed but rotate by an angle of 90° if we pass through $\alpha = 45°$, this has as a consequence that there are two possible orthogonal orientions of the HLG beams with the same l-values. The generated beams are structurally stable on propagation as shown in figure 2.7 apart from slight astigmatism due to imperfect alignment.

[2]For the Matlabcodes to create the simulations we refer to Appendix A.

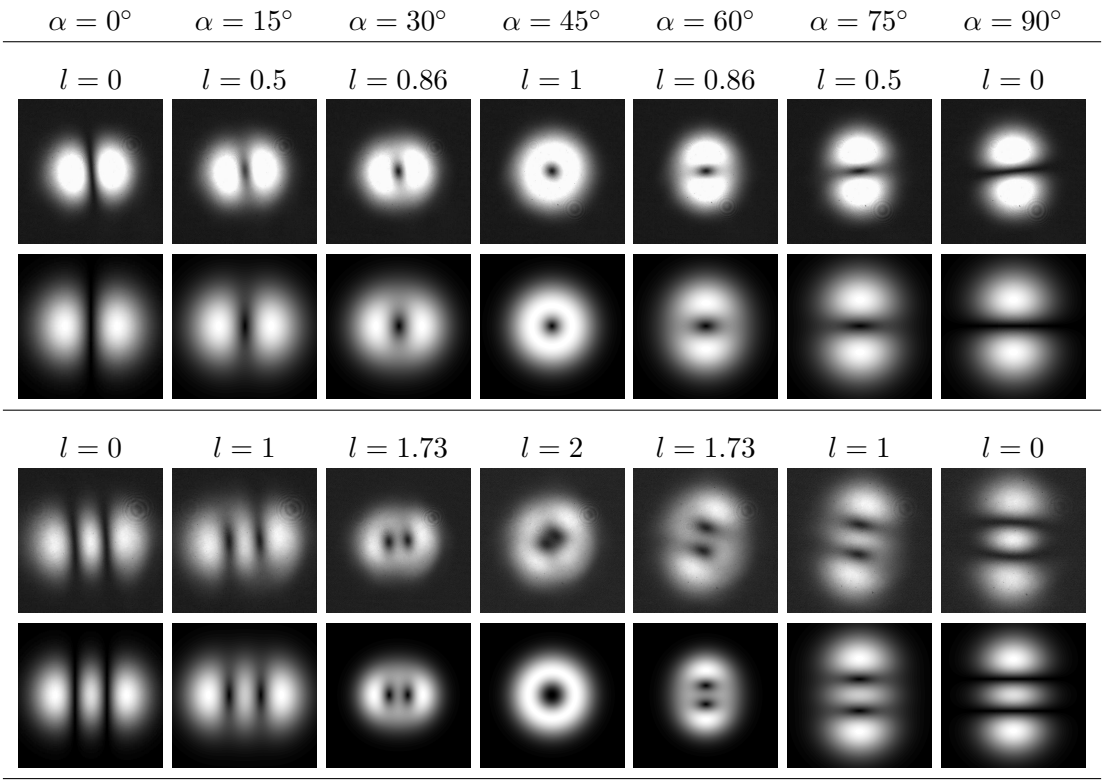

FIGURE 2.8: Results of the beam profile generation. The seven columns correspond to $\alpha = 0°, 15°, 30°, 45°, 60°, 75°, 90°$, carrying OAM values of $l = 0, 0.5, 0.86, 1, 0.86, 0.5, 0$ for the (1,0)-mode and $l = 0, 1, 1.73, 2, 1.73, 1, 0$ for the (2,0)-mode. The four rows correspond to the (1,0)-mode beam profile measurement, (1,0)-mode beam profile simulation, the (2,0)-mode beam profile measurement and (2,0)-mode beam profile simulation, respectively.

2.4 Phase characterization

2.4.1 Experimental Setup

To demonstrate that the phase distribution of our generated beams have the phase distribution of a HLG mode, we interfere our produced beam with a reference beam to obtain an indirect measurement of the phase profile. The setup is shown in figure 2.9. We have split the HG beam with the beam splitter S_1, one arm passes through the mode converter and the collimating lens and forms the beam in the HLG mode as in the previous setup. The other arm functions as the reference beam and is created by diverging the output HG mode by means of a diverging lens with a focal length $f_4 = 200\,mm$ and by tuning the mirrors such that we create a reference beam with only one of the lobes of the beam in HG mode. These two beams are combined by another beam splitter to obtain the interference pattern. To match the intensity of the two

beams, we insert a neutral density filter in the branch of the beam in HLG mode, such that we can obtain a high contrast interference pattern.

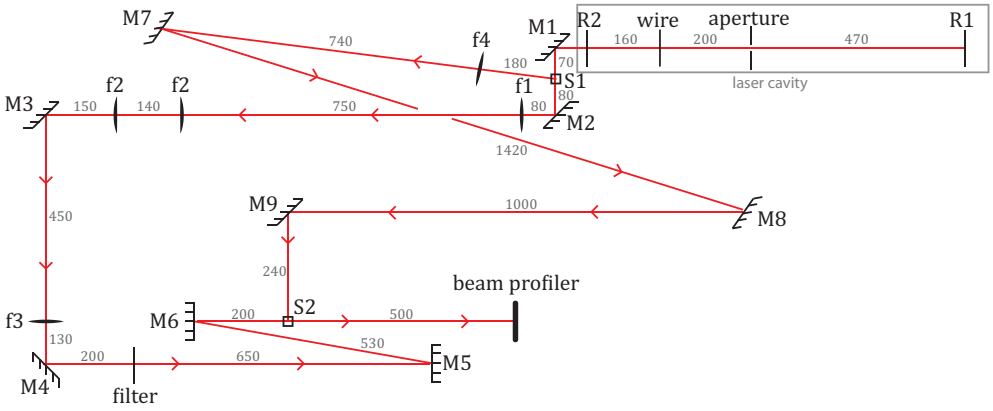

FIGURE 2.9: Experimental setup, viewed from the top, of the interferometer measurement. Part of this setup is the same as in the setup for the intensity characterization. Between M_1 and M_2 there is a beam splitter S_1 that splits the beam into the reference beam arm and into the HLG mode arm. The reference beam is further guided through diverging lens with focal length f_4 and to the second beam splitter S_2 by means of the mirrors M_7 to M_9. Between M_4 and M_5 is a filter to make the beam in HLG mode weaker in intensity and matching the intensity of the reference beam. After M_6 for the one arm and M_9 for the other is the second beam splitter S_2 to recombine both beams and at the end of the laser path is again the CCD device to characterize the created interference pattern.

2.4.2 Results

The calculated phase profile, is shown in the third and sixth row of figure 2.10. We can see in that figure that for the HG modes there is a phasestep of π between the successive lobes and for LG modes there is a continous phase shift in the azimuthal direction that amounts to a total of $l = 2\pi(n - m)$. In the center of the LG mode there is a vortex where the phase is undefined. The HLG modes have similar features. In our interferometer setup we see a grating due to the tilted plane of the reference wave with respect to the beam in HLG mode whWich causes a small phase shift in the projection of the tilted plane onto the plane of the HLG mode. Additionally, a pitchfork structure that branches out to $|n-m|$ arms can be seen for a LG mode, due to the phase dislocation in the center. For HG modes, the respective lobes are shifted by a phase of π which can be seen as a shift in the grating lines. We have measured the interference pattern for the two lowest excited HLG modes: the $(1, 0|\alpha)$-mode and the $(2, 0|\alpha)$-mode.

The analytical description of the HLG modes as in equation (2.12), superimposed with a planar beam under a certain tilt furthermore provide simulations[3]. The results are displayed in figure 2.10.

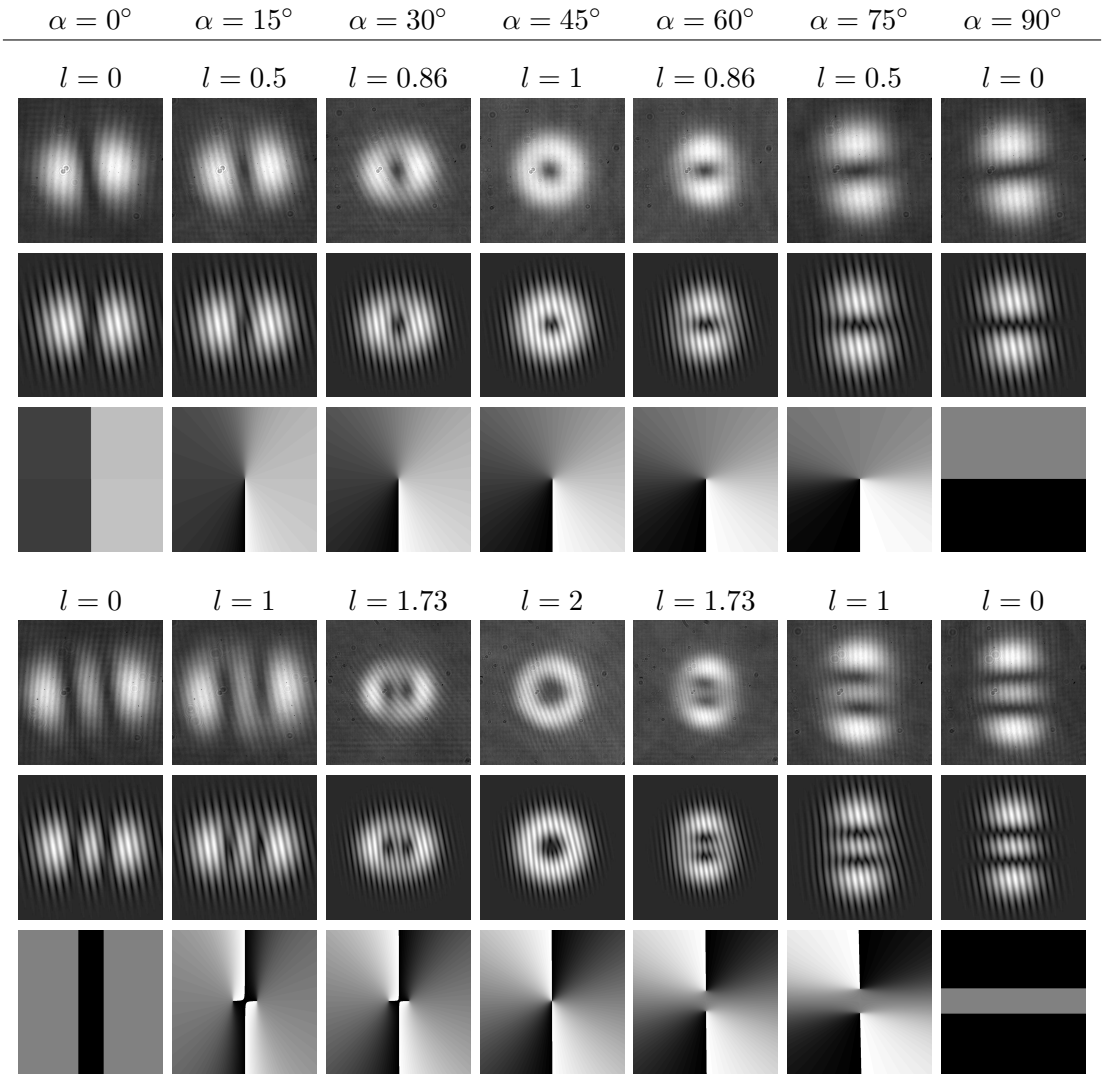

FIGURE 2.10: Results of the interferometer measurements. White and black patches indicate a phase of 2π and 0. The seven columns correspond to $\alpha = 0°, 15°, 30°, 45°, 60°, 75°, 90°$, carrying OAM values of $l = 0, 0.5, 0.86, 1, 0.86, 0.5, 0$ for the (1,0)-mode and $l = 0, 1, 1.73, 2, 1.73, 1, 0$ for the (2,0)-mode. The six rows correspond to the (1,0)-mode interference measurement, (1,0)-mode interference simulation, (1,0)-mode phase profile simulation, (2,0)-mode interference measurement, (2,0)-mode interference simulation and (2,0)-mode phase profile simulation, respectively.

[3]For the Matlabcodes to create the simulations we refer to Appendix A.

2.5 Discussion

The results of the intensity characterization (section 2.3) are virtually identical to their simulated counterparts, that are derived from the analytical solutions, apart from overall scaling. This has been shown in figure 2.8. This is a good indication that our generated beams are indeed HLG modes. Furthermore the results from the phase characterization (section 2.4) also adds up to HLG modes. The pitchfork structure, indicating OAM, is visible in the middle column and first and fourth row of figure 2.10. Although the pitchfork is upside down, when compared to the simulations, the correct number of branches of the pitchfork are visible. The pitchfork is upside down because the tilt of the planar reference beam with respect to the beam in HLG mode, is orientated in a different direction than the tilt in the simulations. If we look at the intermediate HLG-modes the pitchfork structure gradually dissolves to a shift, as expected in the simulations. By characterizing the intensity profile and characterizing the phase profile and verifying these are identical to the profiles predicted by the simulations, we have concluded that we have indeed generated the HLG modes that are described with equation (2.12). Not only do these beams carry non-integer OAM, they are also propagationally stable (figure 2.7). In the generated beams the principle axes of the HLG modes remain fixed when we vary the non-integer OAM, these axes thus also overlap with the quadrant detector measurement axes, which greatly simplifies the general calibration technique, that will be discussed in chapter 3. In our setup the OAM content of the beam in HLG mode can be tuned continuously with the mode orientation angle α, in principle to an arbitrary value $l\hbar$ per photon. An interesting result is that we can create beams that carry the same OAM l per photon but differ in both their phase and intensity distributions as illustrated for the intensity in figure 2.11 for $l = 1$.

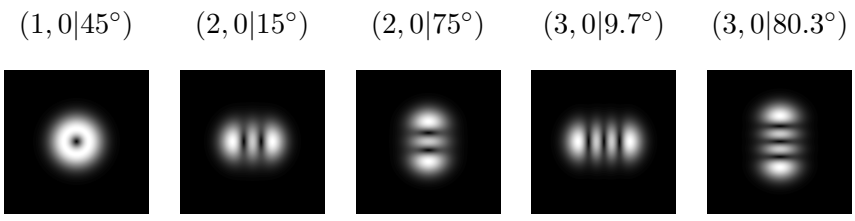

FIGURE 2.11: Example of simulated intensity distributions of different HLG-modes carrying the same OAM. ($l = 1$)

Chapter 3

Positional Measurements Using Quadrant Detectors

3.1 Theory of Quadrant Qetector Response

3.1.1 Quadrant Detector Response

A quadrant detector (QD) is a beam positional measurement device consisting of four photodiodes sorted in an 2x2 array. These four quadrants are equally spaced and are seperated by significantly small gaps of typically less than 0.05% of the active area, as illustrated in figure 3.1. Each of the photodiodes carry a signal current I_A, I_B, I_C, I_D, which is an indication of the total intensity of the impinging beam on the quadrant. The outputs I_x, I_y, I_Σ of the QD are a sum of these signal currents:

$$\begin{aligned} I_x &= I_A - I_B + I_C - I_D \ , \\ I_y &= I_A + I_B - I_C - I_D \ , \\ I_\Sigma &= I_A + I_B + I_C + I_D \ . \end{aligned} \tag{3.1}$$

Analytically, we can write the normalized position-current relation for shifts in the x-direction as:

$$\frac{I_x}{I_\Sigma} = \frac{I_A - I_B + I_C - I_D}{I_A + I_B + I_C + I_D} = \frac{\int_{-a+x}^{x}\int_{-a+y}^{a+y} |U(x,y)|^2\, dydx - \int_{x}^{a+x}\int_{-a+y}^{a+y} |U(x,y)|^2\, dydx}{\int_{-a+x}^{a+x}\int_{-a+y}^{a+y} |U(x,y)|^2\, dydx}\,, \tag{3.2}$$

where a^2 is the total surface area of the quadrant detector and $|U(x,y)|^2$ the intensity of the impinging beam. The center of the beam is in the zero of the coordinate system and the QD is at position (x,y). The integration limits and coordinate system are depicted in Figure 3.1, part (B). The same relation can be found for the y-position by substituting the index x with y. If we confine our beam to well within the quadrant detector this generalizes to:

$$\frac{I_x}{I_\Sigma} = \frac{\int_{-\infty}^{x}\int_{-\infty}^{\infty} |U(x,y)|^2\, dydx - \int_{x}^{\infty}\int_{-\infty}^{\infty} |U(x,y)|^2\, dydx}{\int_{-\infty}^{\infty}\int_{-\infty}^{\infty} |U(x,y)|^2\, dydx}\,. \tag{3.3}$$

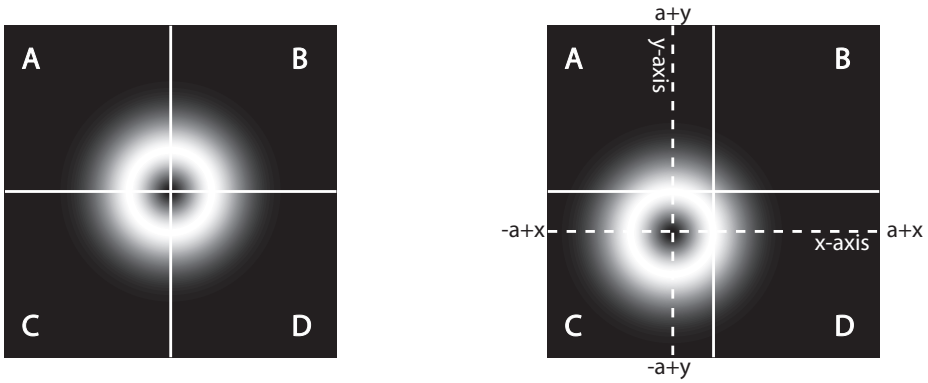

(A) (B)

FIGURE 3.1: A QD detecting a LG beam profile. Part (A) sketches the detector with quadrants A,B,C and D. Part (B) shows the reference frame of the integration corresponding to the displaced QD of equation (3.2).

This is equal to the assumption that the intensity is zero outside the quadrant detector. In solving this integral we take an example of a beam in HLG (1,0)-mode, mathematically expressed in equation (2.13). Solutions for higher order modes can be readily found by

the same method. The solution of the relevant integral is:

$$\begin{aligned}\int_a^b \int_{-\infty}^{\infty} \left|U_{1,0}^{HLG}(x,y|\alpha)\right|^2 dydx &= \int_a^b \int_{-\infty}^{\infty} \left|2\sqrt{2}e^{-x^2-y^2}\left(x\cos\alpha + iy\sin\alpha\right)\right|^2 dydx \\ &= \int_a^b \int_{-\infty}^{\infty} 8e^{-2\left(x^2+y^2\right)}\left(x^2\cos^2\alpha + y^2\sin^2\alpha\right) dydx \\ &= \left[\frac{\pi}{2} erf\left(\sqrt{2}x\right) - \sqrt{2\pi}xe^{-2x^2}\cos^2\alpha\right]_a^b \ . \quad (3.4)\end{aligned}$$

Combining equations (3.4) and (3.2) we find the following analytical expression for the normalized position-current relation:

$$\frac{I_x}{I_\Sigma} = erf\left(\sqrt{2}x\right) - \sqrt{\frac{8}{\pi}}xe^{-2x^2}\cos^2\alpha \ . \quad (3.5)$$

As expected this is a generally non-linear function in x and of α, the HLG mode orientation. The function converges to 1 and -1 at $x = \infty$ and $x = -\infty$ respectively. The function is plotted in the next paragraph in Figure 3.2.

3.1.2 Rotation of symmetry axes

Generally, a HLG mode is not cylindrically symmetric. Although in chapter 2 we have generated the HLG modes such that their symmetry axes remain fixed, it remains interesting to investigate the QD response of arbitrarily orientated symmetry axes. If we rotate the symmetry axes of the HLG mode by θ, which is equal to a change of variables in the Cartesian coordinate system:

$$\begin{bmatrix} x \\ y \end{bmatrix} = \begin{pmatrix} \cos\theta & -\sin\theta \\ \sin\theta & \cos\theta \end{pmatrix} \begin{bmatrix} x' \\ y' \end{bmatrix} \ , \quad (3.6)$$

the rotated analytical expression for the HLG mode becomes:

$$u_{1,0}^{HLG}(x,y|\alpha,\theta) = 2\sqrt{2}e^{-x^2-y^2}(\cos\alpha(x\cos\theta - y\sin\theta) + i\sin\alpha(x\sin\theta + y\cos\theta)) \ . \quad (3.7)$$

Note that we have introduced two notations for two different angles of orientation. The mode orientation α indicates the type of HLG mode, which determines the intensity distribution and OAM value. The angle θ is the angle which the symmetry axes of

the HLG mode make with respect to the x-axis. Using the method of the previous paragraph we found the following normalized position-current relation for arbitrarily orientated HLG modes:

$$\frac{I_x}{I_\Sigma} = erf\left(\sqrt{2}x\right) - \sqrt{\frac{8}{\pi}}xe^{-2x^2}\chi(\alpha,\theta)\ , \tag{3.8}$$

where $\chi(\alpha,\theta) = \cos^2\alpha\cos^2\theta + \sin^2\alpha\sin^2\theta$. This parameter $\chi(\alpha,\theta)$ becomes equal to $1/2$ when α is set to $45°$, which corresponds to the cylindrical symmetry of the LG mode. Interestingly, $\chi(\alpha,\theta)$ also becomes equal to $1/2$ when θ is set to $45°$, this is due to the rectangular symmetry of the HLG mode. Of course, when θ is set to $0°$, equation (3.8) reduces to equation (3.6). Figure 3.2 depicts equation (3.8) for a few settings of α and θ.

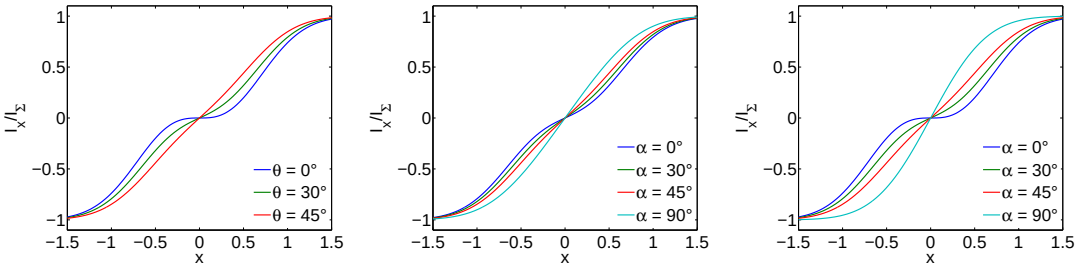

(A) (B) (C)

FIGURE 3.2: This figure plots equation (3.8) for a few settings of α and θ. Part (A) and (B) show plots of $\theta = 0°$ and $\theta = 30°$ respectively, with $\alpha = 0°, 30°, 45°, 90°$. Part (C) shows plots of $\alpha = 0°$ and $\theta = 0°, 30°, 45°$.

3.1.3 Linearity and Calibration Constant

To measure a small displacement $\triangle x \ll w$ with a quadrant detector, the signal obtained from the quadrant detector has to be normalized to the slope of the position-current relation. For there to be a well defined slope it is neccessary to measure in a nearly linear region of the position-current relation. The highest precision for a beam positional measurement will be attained in a region of constant slope (linear region), and the highest sensitivity will be attained for the region with the highest slope. We call the slope of the position-current relation at a point of constant slope the calibration constant K.

For the analytical solution of equation (3.8) there are no regions of constant slope,

only a few isolated locations, where the second derivative of the position-current relation is zero, for which we have calculated the calibration constant. By means of the zeroth order Taylor polynomial of the slope-function around its extreme values we can we can find the maximum error in the calibration constants for displacements near the isolated values of constant slope. This error is proportional to the second derivative of the position-current relation. The first two derivatives of the position-current relation are expressed analytically as:

$$\left(\frac{I_x}{I_\Sigma}\right)'(x) = 2\sqrt{\frac{2}{\pi}}e^{-2x^2}(1-(1-4x^2)\chi(\alpha,\theta)) \ , \tag{3.9}$$

$$\left(\frac{I_x}{I_\Sigma}\right)''(x) = 8\sqrt{\frac{2}{\pi}}e^{-2x^2}(-x+(3x-4x^3)\chi(\alpha,\theta)) \ . \tag{3.10}$$

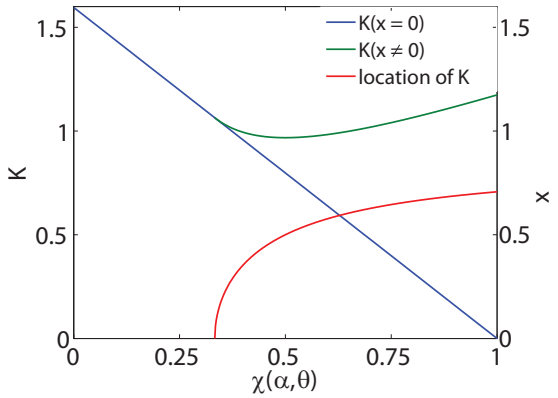

FIGURE 3.3: In this figure the calibration constant K is depicted as a function of χ (blue and green), for the solutions where K is not in the beam center the normalized location of K is also plotted (red).

The calibration constant K is now given by the extreme values of $\left(\frac{I_x}{I_\Sigma}\right)'$. Note that K is dimensionless if we normalize the x-values to the beamwaist. The error of K at locations displaced from the position of K is given by the following Taylor approximation:

$$\zeta(x) \geq \left| x\left(\frac{I_x}{I_\Sigma}\right)''(c)\right| \ , \tag{3.11}$$

with c the location of calibration constant and x the positive, or negative, distance with respect to c. The analytical solutions for the extreme values are:

$$x = 0 \qquad K = \sqrt{\frac{8}{\pi}}(1-\chi) \ , \tag{3.12}$$

and for real values of $\sqrt{3-\frac{1}{\chi}}$, or $\chi \geq \frac{1}{3}$ another set of solutions appear:

$$x = \pm\frac{1}{2}\sqrt{3-\frac{1}{\chi}} \qquad K = 4\sqrt{\frac{2}{\pi}}e^{-\frac{1}{2}(3-\frac{1}{\chi})}\chi \ . \tag{3.13}$$

These functions $x(\chi)$ and $K(\chi)$ have been plotted in figure 3.3. The calibration constant K and its position is also listed for various settings of α and θ in table 3.1. Note that for $\theta = 45°$ or $\alpha = 45°$ the response and, thus, the calibration constant is the same for every mode orientation.

α	$\theta = 0°$		$\theta = 30°$		$\theta = 45°$	
	x	K	x	K	x	K
0°	0	0	0	0.3989	0	0.7979
	0.7071	1.1741	0.6455	1.0403	0.5	0.9679
15°	0	0.1069	0	0.4524	0	0.7979
	0.6942	1.1355	0.6333	1.0253	0.5	0.9679
30°	0	0.3989	0	0.5946	0	0.7979
	0.6455	1.040	0.5916	0.9905	0.5	0.9679
45°	0	0.7979	0	0.7979	0	0.7979
	0.5	0.9679	0.5	0.9679	0.5	0.9679
60°	0	1.1968	0	0.9974	0	0.7979
					0.5	0.9679
75°	0	1.4889	0	1.1434	0	0.7979
					0.5	0.9679
90°	0	1.5958	0	1.1968	0	0.7979
					0.5	0.9679

TABLE 3.1: The calibration constant calculated with equation (3.12) and (3.13) for various settings of α and θ.

3.2 Method

As mentioned in the introduction, a full characterization of the beam profile is required to calibrate the QD for beam positional measurement, this has been the work of chapter 2. The goal of this part of the research is to characterize the position-current relation and to find the calibration constant and the linear area of the position-current relation (as

described in the previous section) for the lowest order HLG (1,0)-mode. The generation method for the beam in HLG mode is equal to the generation method in chapter 2. We have measured the position-current relation of the HLG (1,0)-mode for various settings of α, the mode orientation, and θ, the orientation of its symmetry axes, by placing the QD on a piezo-controlled translation stage and shifting the platform in the x-direction. The device used to shift the platform is the Newport ESP300[26], controlled by a custom-made LabView program. The angle θ of the symmetry axes has been rotated, simply by rotating the quadrant detector itself. These measurements give response profiles of the beam in HLG mode, for which we can calculate the location and value of the calibration constant.

3.3 Experimental setup

For the experiment we have used two different QDs with different size and gain characteristics to compare and understand the effect of different size and gains of the QD in measuring beam position. The Newport QD model 2901[27], has 16 different gain settings listed in table 3.2 and an active area of 3x3 mm. The Newport QD model 2921[28], has only 5 different gain settings listed in table 3.3 and an active area of 10x10 mm. Both QD have three outputs, namely the X, Y and SUM output. For each different gain settings, we obtain different output voltages, due to their different conversion gain factor as listed in the tables. From now on we will refer to these QDs specifically as: model 2901 and model 2921.

To characterize the QD response to the beam in HLG (1,0)-mode we shift the translation stage in the x-direction and measure the response of the X, Y and SUM outputs of the QD with multimeters, respectively the Keithley 197, Fluke 175 and HP34401a multimeters. The stage is shifted from $-1\,mm$ to $+1\,mm$, with steps of $50\,\mu m$, with respect to the beam center, such that the beam with beam waist $w_0 = 545\,\mu m$ is well confined within the left two quadrants and the right two quadrants at the endpoints of the measurement. By using neutral density filters we have kept the power of the beam such that the output of the QD was as near as possible to the upper limit of the SUM output. In this manner we have measured the various combinations of gain settings, α and θ to study the QD response profile of a beam in HLG (1,0)-mode. The setup

Gainsetting	Conversion Gain (X,Y output) ($\lambda = 900\,nm$)	Conversion Gain (SUM output) ($\lambda = 900\,nm$)	Conversion Gain (X,Y output) ($\lambda = 632.8\,nm$)	Conversion Gain (SUM output) ($\lambda = 632.8\,nm$)
$30\,\mu W(10\prime)$	$1000000\,V/W$	$100000\,V/W$	$800000\,V/W$	$80000\,V/W$
$30\,\mu W(10)$	$1000000\,V/W$	$100000\,V/W$	$800000\,V/W$	$80000\,V/W$
$30\,\mu W(3)$	$300000\,V/W$	$100000\,V/W$	$240000\,V/W$	$80000\,V/W$
$30\,\mu W(1)$	$100000\,V/W$	$100000\,V/W$	$80000\,V/W$	$80000\,V/W$
$300\,\mu W(10\prime)$	$100000\,V/W$	$10000\,V/W$	$80000\,V/W$	$8000\,V/W$
$300\,\mu W(10)$	$100000\,V/W$	$10000\,V/W$	$80000\,V/W$	$8000\,V/W$
$300\,\mu W(3)$	$30000\,V/W$	$10000\,V/W$	$24000\,V/W$	$8000\,V/W$
$300\,\mu W(1)$	$10000\,V/W$	$10000\,V/W$	$8000\,V/W$	$8000\,V/W$
$3\,mW(10\prime)$	$10000\,V/W$	$1000\,V/W$	$8000\,V/W$	$800\,V/W$
$3\,mW(10)$	$10000\,V/W$	$1000\,V/W$	$8000\,V/W$	$800\,V/W$
$3\,mW(3)$	$3000\,V/W$	$1000\,V/W$	$2400\,V/W$	$800\,V/W$
$3\,mW(1)$	$1000\,V/W$	$1000\,V/W$	$800\,V/W$	$800\,V/W$
$30\,mW(10\prime)$	$1000\,V/W$	$100\,V/W$	$800\,V/W$	$80\,V/W$
$30\,mW(10)$	$1000\,V/W$	$100\,V/W$	$800\,V/W$	$80\,V/W$
$30\,mW(3)$	$300\,V/W$	$100\,V/W$	$240\,V/W$	$80\,V/W$
$30\,mW(1)$	$100\,V/W$	$100\,V/W$	$80\,V/W$	$80\,V/W$

TABLE 3.2: QD model 2901 gain settings. For this model there is a difference between the X,Y and SUM output in the conversion gain factor. The responsivity at the operating wavelength is lower than the listed values in the manual[28] by a factor of $\frac{4}{5}$ (this factor is also taken from the manual).

Gainsetting	Conversion Gain ($\lambda = 900\,nm$)	Conversion Gain ($\lambda = 632.8\,nm$)	Sum Range ($\lambda = 632.8\,nm$)
$50\,\mu W$	$100000\,V/W$	$66667\,V/W$	0-3 V
$150\,\mu W$	$33300\,V/W$	$20000\,V/W$	0-3 V
$500\,\mu W$	$10000\,V/W$	$6667\,V/W$	0-3 V
$1.5\,mW$	$3333\,V/W$	$2000\,V/W$	0-3 V
$5\,mW$	$1000\,V/W$	$667\,V/W$	0-3 V

TABLE 3.3: QD model 2921 gain settings. For this model there is no difference between the X,Y and SUM output. The responsivity at the operating wavelength is lower than the listed values in the manual[28] by a factor of $\frac{2}{3}$ (this factor is also taken from the manual).

depicted in figure 3.4 is almost identical to the setup of the previous chapter in figure 2.6.

3.4 Results

3.4.1 Position-current relation

The measurements described in the previous section for the (1,0)-mode HLG beam have been plotted, together with the simulations provided by the analytical solution of equation (3.8) in figure 3.5 and in figure 3.6. The former compares the response for the

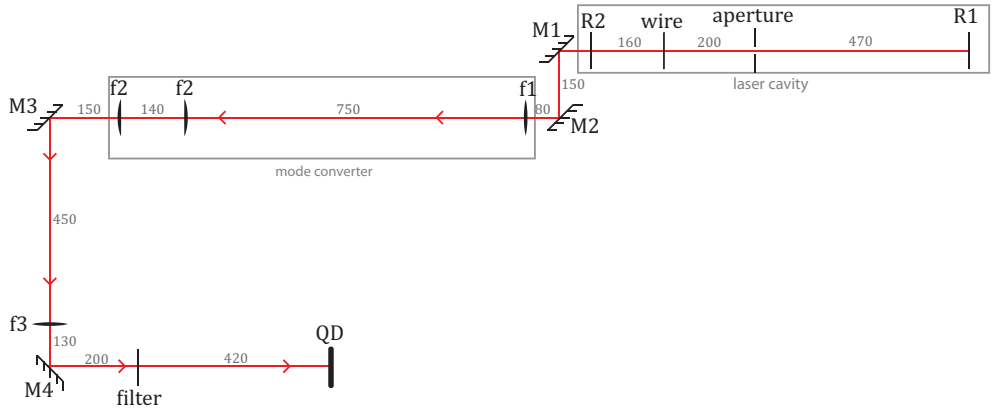

FIGURE 3.4: Experimental setup of QD response measurement. The setup is identical to the setup in Chapter 3.1, but instead of a CCD there is a QD place on a motion controlled platform. Optionally, we use a neutral density filter to prevent saturation of the detector.

two different QD and their gain settings, and the latter compares the QD response for various settings of α and θ. There are three data plots that do not exactly follow the simulation, due to the low intensity of the laserbeam and background room illumination. These are the measurements of model 2901 at gain setting $30\,\mu W(1)$ and of model 2921 at gain setting $50\,\mu W$ and at gain setting $150\,\mu W$.

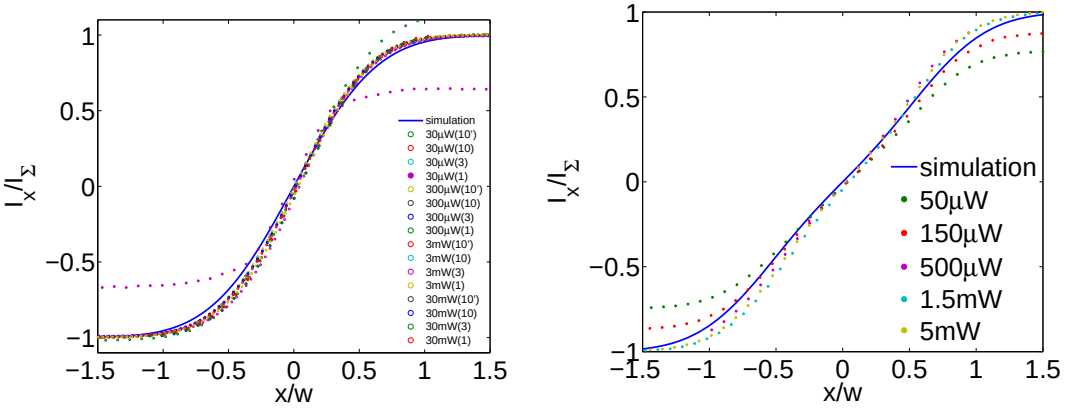

(A) Model 2901 measured at variable gain settings and $\alpha = \theta = 0°$.

(B) Model 2921 measured at variable gain settings, $\alpha = 45°$ and $\theta = 0°$.

FIGURE 3.5: QD response results for a HLG (1,0)-mode. These figures show the response intensity $\frac{I_x}{I_\Sigma}$ plotted against the displacement normalized to the beam waist. In this figure the two models and their gain settings are compared. The solid lines represent simulations and the dots represent measurements in all figures.

The response is identical for either $\alpha = 0°, \theta = 30°$ and $\alpha = 30°, \theta = 0°$ which can be seen in equation (3.8), and also when we compare the blue line in part (B) of figure 3.6

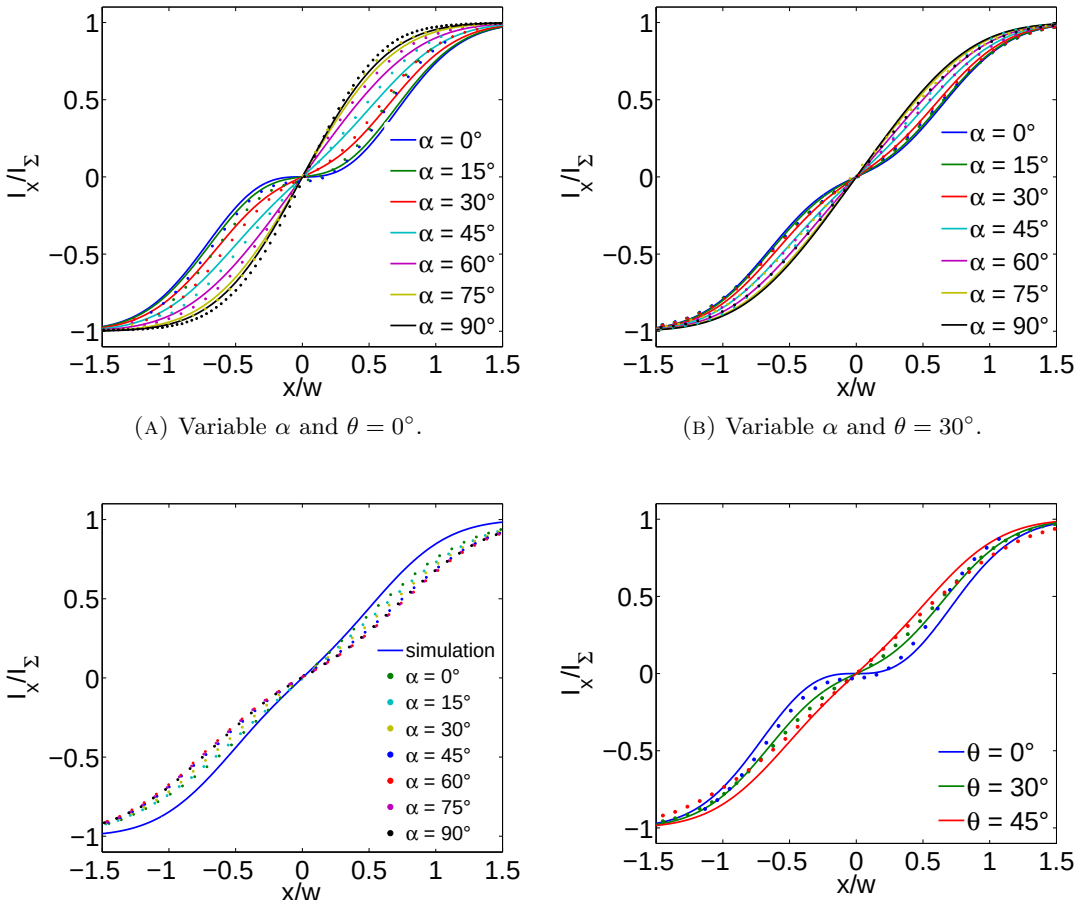

(A) Variable α and $\theta = 0°$.

(B) Variable α and $\theta = 30°$.

(C) Variable α and $\theta = 45°$.

(D) Orientation angle $\alpha = 0°$ and variable θ.

FIGURE 3.6: QD response results of model 2901 on setting 300 μW(3) for a HLG (1,0)-mode. These figures show the response intensity I_x/I_Σ plotted against the displacement normalized to the beamwaist and comparing different settings of α and θ. The solid lines represent simulations and the dots represent measurements in all figures.

with the green line in part (D) of the same figure. There is also only one simulation possible for $\theta = 45°$, illustrated in part (C) of said figure, meaning that the response for all mode orientations of the HLG (1,0)-mode are identical for $\theta = 45°$.

3.4.2 Calibration Constant

To recall: the calibration constant is the value of the slope of the position-current relation, at a position of constant slope. We have calculated the position and values of the calibration constant for the HLG (1,0)-mode with equations (3.12) and (3.13). These calculated values will serve as simulations. The *calculated* position will be taken as the position of the *measured* calibration constant. The measured calibration constant will

be determined (on its calculated position) by central differentiation of the measured datapoints. The results are illustrated in figure 3.7 and summarized in figure 3.8.

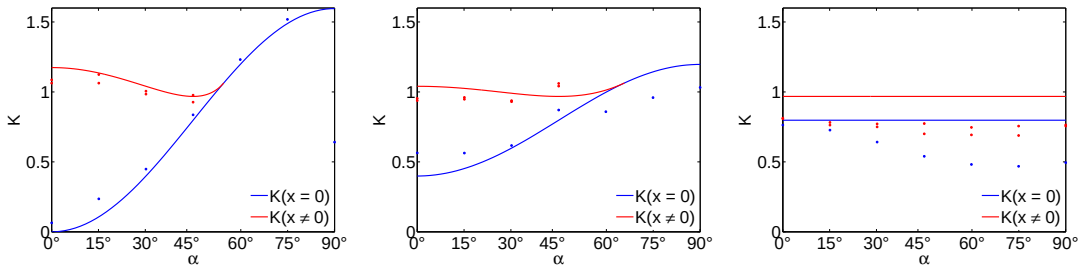

(A) (B) (C)

FIGURE 3.7: This figure plots equation (3.12) and (3.13) for a few settings of α and θ. Part (A),(B) and (C) show plots of $\theta = 0°$, $\theta = 30°$ and $\theta = 45°$ respectively. Dots indicate measured values and solid lines indicate calculations.

Each subfigure in figure 3.7 contains three datasets (dots) and simulations (solid lines), and they plot the calibration constant against the mode orientation α. One dataset for the centered location and two dataset for the two locations off the center. Note that the simulation for $\theta = 45°$ predicts a constant calibration factor, which is not entirely obtained in the measurement: The slope is nearly constant, but is lower than predicted. Figure 3.8 summarizes all datasets into one figure, where the calibration constant is plotted against the parameter $\chi(\alpha, \theta)$ from section 3.1.3. The line of datapoints visible at $\chi = 0.5$ is due to the measurement at $\theta = 45°$.

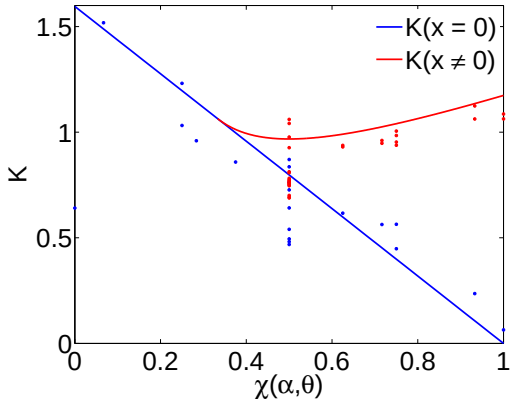

FIGURE 3.8: In this figure the calibration constant K is depicted as a function of χ. Dots indicate measured values and solid lines indicate calculations.

3.5 Discussion

In this chapter we have presented a general quadrant detector calibration technique for non-integer OAM beams in HLG modes. Starting from the analytical solutions of HLG (1,0)-mode found in chapter 2 we have derived the position-current relation, the calibration constant K and its location for this mode. These position-current relations and values of K have been verified experimentally. The position-current relation is dependent on the gain settings of the particular quadrant detector, the orientation θ of the symmetry axis of the beam in HLG mode and the mode orientation α of the beam in HLG mode.

Deviations from analytical solutions of the position-current relation can be a result of: (i) Background light in the case of a very high gain setting as can be seen for the highest gain settings in figure 3.5. The position-current relation takes the following form in such case: $I_x/(I_\Sigma + c)$ where c is the background illumination. (ii) Misalignments of orientations α and θ as can be seen very well in part (C) of figure 3.6. This misalignment error is enlarged by the calculation of the calibration constant for $\theta = 45°$. In part (C) of figure 3.7 the slope is too low due to the misalignment. Apart from these small problems the position-current relation and the calibration constant are the same analytically and experimentally, verifying our method.

An important feature of the position-current relation is its general non-linearity, for that reason the calibration constant K is not constant for all locations of the non-isotropic beam. We have sought and found the ideal locations in the beam for which the calibration constant is high and the position-current relation nearly linear. This location was found to be off center for $\chi \leq 1/3$, with values as in table 3.1. A consequence of this is that the quadrant detector is most sensitive for these beams at locations off the center of the beam.

Chapter 4

Conclusion

We have generated non-integer orbital angular momentum beams in Hermite-Laguerre-Gaussian modes by using astigmatic mode converters. The generated beams have fixed symmetry axes and are propagationally invariant. Furthermore, our method allows for continuous tuning of the orbital angular momentum value. The correspondence with analytical Hermite-Laguerre-Gaussian modes in intensity and phase has been experimentally verified. Thus, we have provided a general method to generate non-integer orbital angular momentum beams in Hermite-Laguerre-Gaussian modes, with the same order as the input Hermite-Gaussian modes.

The quadrant detector response of our generated Hermite-Laguerre-Gaussian modes has been investigated both analytically and experimentally. A general calibration technique has been described and demonstrated for the first order excited Hermite-Laguerre-Gaussian mode. The influence of the gain settings and of the rotation of the symmetry axes of the Hermite-Laguerre-Gaussian modes has also been investigated. To conclude: Both the Hermite-Laguerre-Gaussian mode orientation and orientation of the symmetry axes of the Hermite-Laguerre-Gaussian mode play an important role in the quadrant detector response. Furthermore, the anisotropic nature of the Hermite-Laguerre-Gaussian has as a result that the quadrant detector is generally not the most sensitive in the center of the beam. The results of both the generation technique and quadrant detector calibration can be extended to higher order Hermite-Laguerre-Gaussian modes carrying (higher) non-integer orbital angular momentum.

Appendix A

Matlab Simulation Codes

A.1 HG mode simulation

The following code to simulate HG modes, with $(n, m) = (8, 5)$, produces the result shown in figure A.1 if we plot the absolute values of the u_{HG}.

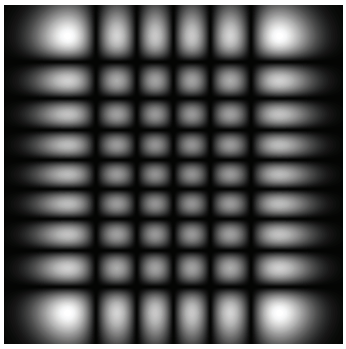

FIGURE A.1:

```
%% Some general quantities
b_0 = (pi/lambda)*w_0^2;              %Rayleigh range
k = 2*pi/lambda;                     %Wavenumber
w = sqrt(2*k*b_0);                   %Beamwaist
N = n+m;

% Hermite polynomial creator (Rodriguez formula)
function [H] = Hermite(n,y)
  H = zeros(size(y));
  if (n > -1)
     syms x;
```

```
     Her = (-1)^n * exp(x^2)*diff(exp(-x^2),x,n);
     Her = simplify(Her);
     H = polyval(sym2poly(Her),y);
  end
end

function [u_HG] = HG_mode(n,m,x,y,w_0,lambda)

 %creating HG_mode
 C_HG = sqrt(2/(pi*factorial(m)*factorial(n)))*2^(-N/2);
 C2_HG = (1/w)*exp(-(x.^2+y.^2)/w^2);
 [HGn] = Hermite(n,x*(sqrt(2)/w));
 [HGm] = Hermite(m,y*(sqrt(2)/w));

 u_HG = C_HG.*C2_HG.*HGn.*HGm;
end
```

A.2 LG mode simulation

The following code to simulate LG modes, with $(n, m) = (8, 5)$, produces the result shown in figure A.2 if we plot the absolute values of the u_{LG}.

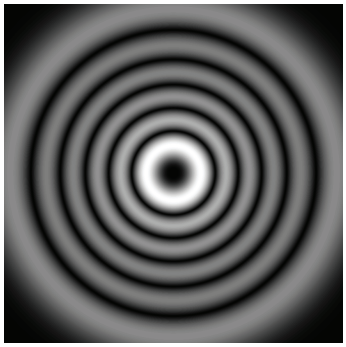

FIGURE A.2:

```
% Laguerre polynomial creator (Rodriguez formula)
function [L] = Laguerre(p,l,y)
     L = zeros(size(y));
  if (p > 0)
     syms x;
     Lag = (x^(-l)*exp(x))/factorial(p) * diff(exp(-x)*x^(p+l),x,p);
     Lag = simplify(Lag);
     L = polyval(sym2poly(Lag),y);
  elseif (p == 0)
     L = ones(size(y));
  end
end
```

```
% LG mode creator
function [u_LG] = LG_mode(n,m,r,w_0,lambda)
 %derived quantities
 l = abs(n-m);
 p = min(n,m);

 % creating LG_mode
 C_LG = sqrt(2/(pi*factorial(m)*factorial(n)))*factorial(p);
 C2_LG = (1/w)*exp(-r.^2/w^2);
 C3_LG = (-1)^p*(sqrt(2).*r/w).^(l);
 [LGpl] = Laguerre(p,l,2.*r.^2/(w^2));

 u_LG = C_LG.*C2_LG.*C3_LG.*LGpl;
end
```

A.3 HLG mode simulation

The following code to simulate HLG modes, with $(n, m) = (8, 5), \alpha = 15$ degrees, produces the result shown in figure A.3 if we plot the absolute values of the u_{HLG}.

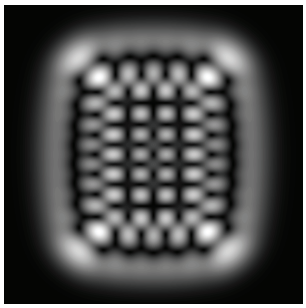

FIGURE A.3:

```
function P_j = Jacobi2(n,alpha,beta,x)
if(n<0)
    P_j = 0;
else
    m = 0:n;
    c = exp(gammaln(n+alpha+1)+gammaln(n+beta+1)-gammaln(m+1)
      - gammaln(n-m+1)-gammaln(n+alpha-m+1)-gammaln(beta+m+1));
    P_j = 2^(-n)*sum(c.*(x-1).^(n-m).*(x+1).^m);
end

function [u_HLG]= HLG_mode(m,n,x,y,w_0,lambda,alpha)
if (alpha == 0) alpha = 0.00001; end  %alpha = 0 doesn't work

%derived quantities
alpharad= alpha * pi/180;             %Astigmatic angle
```

```
alpharot= -cos(2*alpharad);
kappa=[0:1:N];                      %Jacobian polynomial orde

% creating HLG mode
HLG = zeros(size(x));
for i = 1:length(kappa);
    mu = m-kappa(i);
    nu = n-kappa(i);
    P_k = Jacobi2(kappa(i),mu,nu,alpharot);
    HGx = Hermite(N-kappa(i),sqrt(2).*x/w);
    HGy = Hermite(kappa(i),sqrt(2).*y/w);
    fac = (1j)^(kappa(i))*(cos(alpharad))^(mu)*(sin(alpharad))^(nu);
    HLG = HLG + fac.*P_k.*HGx.*HGy;
end

C_HLG = sqrt(1/(pi*factorial(m)*factorial(n))*2^(1-N));
C2_HLG =(1/w)*exp(-(x.^2+y.^2)/w^2);

u_HLG = C_HLG.*C2_HLG.*HLG;
end
```

A.4 plane wave simulation

The following code simulates the planar wave in the interferometer setup:

```
function [u_plane]= plane_mode(x,y,w_0,lambda,tiltx,tilty,u_HLG,del_int)
tiltx_rad = tiltx*pi/180;           %Tilt compared to u_HLG
tilty_rad = tilty*pi/180;

% creating tilted plane mode
amp = del_int*max(max(abs(u_HLG)));   %Scale with u_HLG
u_plane = amp*exp(1j*(x*sin(tiltx_rad)+y*sin(tilty_rad)));
end
```

Appendix B

A.M. Nugrowati, W.G. Stam, J.P. Woerdman, "Position measurement of non-integer OAM beams with structurally invariant propagation"

This is a paper published in ArXiv and is based partly on work of this thesis. See also for the most updated version: http://arxiv.org/abs/1207.6019

Position measurement of non-integer OAM beams with structurally invariant propagation

A. M. Nugrowati, W. G. Stam and J. P. Woerdman

Huygens Laboratory, Leiden University, P.O. Box 9504, 2300 RA Leiden, NL
**Corresponding author: nugrowati@physics.leidenuniv.nl*

Abstract: We present a design to generate structurally propagation invariant light beams carrying non-integer orbital angular momentum (OAM) using Hermite-Laguerre-Gaussian (HLG) modes. Different from previous techniques, the symmetry axes of our beams are fixed when varying the OAM; this simplifies the calibration technique for beam positional measurement using a quadrant detector. We have also demonstrated analytically and experimentally that both the OAM value and the HLG mode orientation play an important role in the quadrant detector response. The assumption that a quadrant detector is most sensitive at the beam center does not always hold for anisotropic beam profiles, such as HLG beams.

OCIS codes: 040.5160, 120.4640, 260.6042.

References and links

1. E. Abramochkin and V. Volostnikov, "Beam transformation and nontransformed beams," Opt. Commun. **83**, 123–125 (1991).
2. L. Allen, M. W. Beijersbergen, R. J. C. Spreeuw, and J. P. Woerdman, "Orbital angular momentum of light and the transformation of Laguerre-Gaussian laser modes," Phys. Rev. A **45**, 8185–8189 (1992).
3. H. He, N. R. Heckenberg, and H. Rubinsztein-Dunlop, "Optical particle trapping with higher-order doughnut beams produced using high efficiency computer generated holograms," J. Mod. Opt. **42**, 217–223 (1995).
4. M. Padgett and R. Bowman, "Tweezers with a twist," Nat. Photon **5**, 343–348 (2011).
5. S. S. R. Oemrawsingh, X. Ma, D. Voigt, A. Aiello, E. R. Eliel, G. W. 'tHooft, and J. P. Woerdman, "Experimental demonstration of fractional orbital angular momentum entanglement of two photons," Phys. Rev. Lett. **95**, 240501 (2005).
6. B. J. Pors, F. Miatto, G. W. 't Hooft, E. R. Eliel, and J. P. Woerdman, "High-dimensional entanglement with orbital-angular-momentum states of light," J. Opt. **13** (2011).
7. J. Sato, M. Endo, S. Yamaguchi, K. Nanri, and T. Fujioka, "Simple annular-beam generator with a laser-diode-pumped axially off-set power build-up cavity," Opt. Commun. **277**, 342–348 (2007).
8. G. C. G. Berkhout and M. Beijersbergen, "Measuring optical vortices in a speckle pattern using a multi-pinhole interferometer," Opt. Express **18** (2010).
9. F. Tamburini, B. Thidé, G. Molina-Terriza, and G. Anzolin, "Twisting of light around rotating black holes," Nat. Phys. **7**, 195–197 (2011).

10. M. Merano, N. Hermosa, J. P. Woerdman, and A. Aiello, "How orbital angular momentum affects beam shifts in optical reflection," Phys. Rev. A **82** (2010).
11. M. W. Beijersbergen, L. Allen, H. E. L. O. van der Veen, and J. P. Woerdman, "Astigmatic laser mode converters and transfer of orbital angular momentum," Opt. Commun. **96**, 123–132 (1993).
12. M. W. Beijersbergen, R. P. C. Coerwinkel, M. Kristensen, and J. P. Woerdman, "Helical-wavefront laser beams produced with a spiral phaseplate," Opt. Commun. **112**, 321–327 (1994).
13. G. A. Turnbull, D. A. Robertson, G. M. Smith, L. Allen, and M. J. Padgett, "The generation of free-space Laguerre-Gaussian modes at millimetre-wave frequencies by use of a spiral phaseplate," Opt. Commun. **127**, 183–188 (1996).
14. J. Arlt, K. Dholakia, L. Allen, and M. J. Padgett, "The production of multiringed Laguerre-Gaussian modes by computer-generated holograms," J. Mod. Opt. **45**, 1231–1237 (1998).
15. L. Marrucci, C. Manzo, and D. Paparo, "Optical spin-to-orbital angular momentum conversion in inhomogeneous anisotropic media," Phys. Rev. Lett. **96** (2006).
16. G. Machavariani, N. Davidson, E. Hasman, S. Bilt, A. Ishaaya, and A. A. Friesem, "Efficient conversion of a Gaussian beam to a high purity helical beam," Opt. Commun **209**, 265–271 (2002).
17. S. A. Kennedy, M. J. Szabo, H. Teslow, J. Z. Porterfield, and E. R. I. Abraham, "Creation of Laguerre-Gaussian laser modes using diffractive optics," Phys. Rev. A **66**, 043801 (2002).
18. S.-C. Chu and K. Otsuka, "Doughnut-like beam generation of Laguerre-Gaussian mode with extremely high mode purity," Opt. Commun. **281**, 1647–1653 (2008).
19. N. Matsumoto, T. Ando, T. Inoue, Y. Ohtake, N. Fukuchi, and T. Hara, "Generation of high-quality higher-order Laguerre-Gaussian beams using liquid-crystal-on-silicon spatial light modulators," J. Opt. Soc. Am. A **25**, 1642–1651 (2008).
20. T. Ando, Y. Ohtake, N. Matsumoto, T. Inoue, and N. Fukuchi, "Mode purities of Laguerre–Gaussian beams generated via complex-amplitude modulation using phase-only spatial light modulators," Opt. Lett **34**, 34–36 (2009).
21. M. V. Berry, "Optical vortices evolving from helicoidal integer and fractional phase steps," J. Opt. A: Pure Appl. Opt. **6**, 259–268 (2004).
22. J. B. Götte, K. O'Holleran, D. Preece, F. Flossman, S. Franke-Arnold, S. M. Barnett, and M. J. Padgett, "Light beams with fractional orbital angular momentum and their vortex structure," Opt. Express **16** (2008).
23. D. P. O'Dwyer, C. F. Phelan, Y. P. Rakovich, P. R. Eastham, J. G. Lunney, and J. F. Donegan, "Generation of continuously tunable fractional optical orbital angular momentum using internal conical diffraction," Opt. Express **18**, 16480 – 16485 (2010).
24. A. T. O'Neil and J. Courtial, "Mode transformations in terms of the constituent Hermite-Gaussian or LaguerreGaussian modes and the variable-phase mode converter," Opt. Commun. **181**, 35–45 (2000).
25. E. G. Abramochkin and V. G. Volostnikov, "Generalized Gaussian beams," J. Opt. A: Pure Appl. Opt. **6**, S157–S161 (2004).
26. J. Visser and G. Nienhuis, "Orbital angular momentum of general astigmatic modes," Phys. Rev. A **70**, 013809 (2004).
27. E. G. Abramochkin, E. Razueva, and V. G. Volostnikov, "General astigmatic transform of Hermite-Laguerre-Gaussian beams," J. Opt. Soc. Am. A **27**, 2506–2513 (2010).
28. E. J. Lee, Y. Park, C. S. Kim, and T. Kouh, "Detection sensitivity of the optical beam deflection method characterized with the optical spot size on the detector," Curr. Appl. Phys. **10**, 834–837 (2010).
29. Y. Panduputra, T. W. Ng, A. Neild, and M. Robinson, "Intensity influence on Gaussian beam laser based measurements using quadrant photodiodes," Appl. Opt. **49** (2010).
30. N. Hermosa, A. Aiello, and J. P. Woerdman, "Quadrant detector calibration for vortex beams," Opt. Lett. **36** (2011).
31. We thank Steven Habraken for this idea.

1. Introduction

Light carrying orbital angular momentum (OAM) is characterized by a helical wavefront shape and a doughnut-like intensity profile with a dark center (vortex). In a single round trip about the propagation axis, the phase of an OAM beam increases linearly and gains the value of $2\pi N$, with N an integer value that is equivalent to the OAM content of such a beam. After the first investigation of the astigmatic transformation of Hermite-Gaussian (HG) modes into Laguerre-Gaussian (LG) modes [1], it was theoretically proven that LG laser modes carry a well defined OAM which is equivalent to the azimuthal mode index ℓ of the LG modes [2]. Since then, the generation of LG modes has opened up a broad range of applications, including optical trapping with OAM beam structures [3, 4], quantum communication at higher dimensional entanglement using OAM beams [5, 6], OAM beam for high sensitivity Raman spectroscopy in molecule detection [7], stellar detection using OAM beam [8, 9], and nanometer precision metrology by using the effect of OAM on beam shifts [10].

Recently, there is a growing interest in addressing *non-integer* values of OAM that potentially broadens the OAM beams applications. This will be the topic of our paper. We present the technique to generate non-integer OAM beams and discuss the difference between our technique and the existing ones. Subsequently, we treat the position measurement of such a beam that is an inherent part of many applications using OAM beams.

During the first decade after the initial realization of an OAM beam, many different *integer* OAM beam generation techniques have been introduced. The first demonstration used the so-called '$\pi/2$-mode converter', which belongs to a family of astigmatic mode converters that applies the appropriate Gouy phase to create well defined mode indices of LG beams carrying integer OAM [11]. This was soon followed by the demonstration of a spiral phase plate (SPP) operating at optical wavelength [12] and at milimeter range [13] for creating helical-wavefront to directly transform Gaussian beam to OAM beams. At the same time, computer-generated holograms with pitchfork structures were applied using a spatial light modulator (SLM) to convert Gaussian beams into LG beams [3, 14]. Different from the astigmatic mode converter, both SPP and SLM are not pure mode converters. They convert a fundamental Gaussian mode into a superposition of LG modes that contain the same azimuthal mode index ℓ but different radial mode index p. Although the OAM content of such a beam is well defined, the spatial field distribution evolves during propagation. This mode impurity problem holds also when employing q plates [15] that convert spin-to-orbital angular momentum in an anisotropic and inhomogeneous media to create helical waves. Mitigating the radial mode impurity to obtain a more robust beam profile during propagation when using SLM and SPP has then been the focus of several studies [16, 17, 18, 19, 20].

In the field of *non-integer* OAM beam generation, only a handful of studies have been carried on. One of the initial ideas was to use off-axis illumination of an SPP; equivalently, one may use a non-integer 2π phase step SPP [5]. These techniques, however, yield non-integer OAM beams with neither ℓ nor p mode purity [21]. A more structurally stable non-integer OAM beam has been demonstrated recently, by using

an SLM when applying a synthesis of a finite number of LG modes with carefully chosen Gouy phases [22]. It was, however, demonstrated only for half-integer OAM values. Another proposition is by exploiting the internal conical diffraction where a circularly polarized beam with a fundamental Gaussian mode is converted into a non-integer OAM beam with a Bessel mode, having only a limited OAM value range of $|\ell| \leq 1$ [23].

Our paper focuses on two issues. The first concerns with the generation of beams carrying arbitrary non-integer OAM values that is structurally stable during propagation. This can be achieved by employing the concept of generally astigmatic mode converters, as was initially introduced in Ref. [24]. Later on, it was theoretically demonstrated that the output of a general astigmatic transformation is the intermediate beam between HG and LG beams, known as Hermite-Laguerre-Gaussian (HLG) beams [25, 26, 27]. Since such a HLG mode is an analytic interpolation between a HG mode and a LG mode, it is structurally propagation invariant. Moreover, this HLG beam carries non-integer OAM.

The second issue concerns with the positional detection of generated HLG modes for applications of non-integer OAM beams, e.g. in precision metrology, optical tweezing or scanning near-field optical microscopy. Popular device to measure beam position is a quadrant detector, made of 2 by 2 array of photodiodes that are equally spaced and produce four electronic signals that are proportional to the beam position. The sensitivity of the position measurement using a quadrant detector is limited within a small spatial range, where the detector response to the shift of the beam is linear. This holds even for the position detection of a typical fundamental Gaussian beam. The non-linear response of a quadrant detector has been addressed and improved, but only for fundamental Gaussian beams [28, 29]. Recently, we have also investigated the response and correspondingly the calibration of a quadrant detector for LG modes carrying *integer* OAM beams [30]. In this paper, we are going to discuss the use of a quadrant detector for beam positional detection *non-integer* OAM beams based upon HLG modes.

We start our paper by presenting the design of a mode converter which transforms a HG mode of arbitrarily high order to a HLG mode [25]. We demonstrate that the output beam is structurally propagation invariant, and characterize the non-integer OAM value using an interferometer set-up. Different from the previous designs [24, 25], our experimental set-up generates HLG beam with fixed symmetry axes when varying the non-integer OAM; these axes thus also overlap with the quadrant detector measurement axes. This proves to be very beneficial when detecting the beam position of HLG modes as shown in the second part of the paper. Further, we derive an analytical expression of a quadrant detector response towards general astigmatic modes and introduce a calibration procedure required for detecting the positional shifts of non-integer OAM beams.

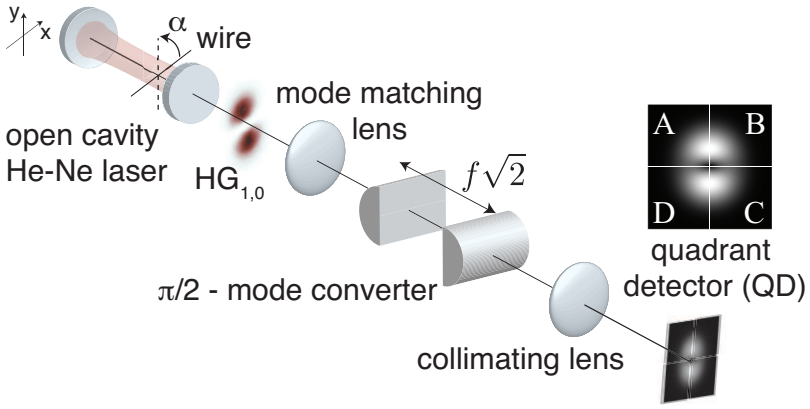

Fig. 1. Our experimental set-up to generate HLG modes as non-integer OAM beams, equipped with a quadrant detector for measuring the beam positional shifts, discussed in Section 3.

2. Generation of structurally propagation invariant light carrying non-integer OAM

2.1. Experimental set-up

A conventional $\pi/2$ astigmatic mode converter [11] transforms a pure HG mode into a pure LG mode by passing an incoming HG beam through a pair of identical cylindrical lenses with focal lengths f, separated at a distance $d = f\sqrt{2}$, as illustrated in Figure 1. A mode matching lens is normally used to tailor the beam waist of the outgoing laser mode into the desired beam waist in between the cylindrical lens. A well defined *integer* OAM is achieved when the symmetry axes of the HG beam are oriented at an angle $\alpha = 45^{\text{o}}$ with respect to the symmetry axes of the cylindrical lenses [11]. This can be done using an open laser cavity that is forced to operate at a high order HG mode by insertion of a thin metal wire, oriented at $\alpha = 45^{\text{o}}$.

Belonging to the family of astigmatically transformed HG beams, HLG beams can be created by tuning the beam parameter α, i.e. the angle between the symmetry axes of cylindrical lenses and the symmetry axes of the input HG beam [27]. The non-integer OAM value of HLG beam is $\ell = (n-m)\sin 2\alpha$, with n and m the mode index of high order HG beams [25, 26]. Another way to generate HLG beams is to tailor the required Gouy phase by simultaneously tuning the separation distance of the cylindrical lenses d and the position of the cylindrical lenses pair with respect to the mode matching lens [31]. However, for aligning purposes, the approach of varying α is more attractive when tuning the non-integer OAM value.

A general astigmatic mode converter transforms a HG mode of arbitrarily high order to a HLG mode. In essence, a pure mode transformation projects an incoming HG mode into two orthogonal axes of the astigmatic mode converter. The outgoing HLG beam is a superposition of the projected mode with the additional Gouy phase. In Figure 2, we

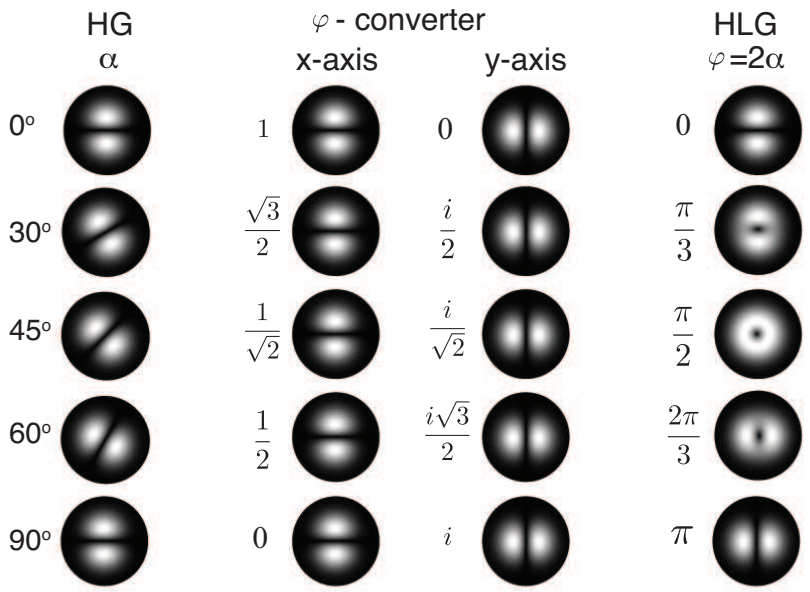

Fig. 2. An incoming $HG_{0,1}$ mode at varying orientation angle α projected onto the orthogonal symmetry axes of the cylindrical lenses of a '$\pi/2$-mode converter'. The symmetry axes of the outgoing HLG modes are always aligned to the projection axes. The outgoing HLG modes experience Gouy phase $\varphi = 2\alpha$.

show the projection of an incoming HG_{01} mode with varying orientation angle α on a '$\pi/2$-mode converter'. The Gouy phase φ experienced by the projected mode after traversing the cylindrical lenses is 2α. Note that the symmetry axes of the outgoing HLG beam are always aligned to the projection axes of the cylindrical lenses.

In this paper, we demonstrate the non-integer OAM beam generation using a HeNe gain tube (Spectra Physics 120S) operating at a wavelength $\lambda = 632.8$ nm, situated at the centre of an open two-mirror cavity allowing for a generation of up to the third order of the HG mode family (i.e. $HG_{3,3}$). The laser is forced to operate in a single higher order HG mode by insertion of a 18 μm diameter copper wire normal to and rotatable with respect to the axis of the laser cavity. The strength and location of a mode matching lens and a pair of cylindrical lenses are chosen such that they create integer OAM beams when the wire is orientated at $\alpha = 45^{o}$. By rotating the wire about the optical axis, we tune the parameter α to generate the HLG modes. This is different from the two previous techniques; where two Dove prisms and two cylindrical lenses are rotated to flip the HG mode before being converted into HLG modes [24], or where α is tuned by rotating the cylindrical lenses [25]. By rotating the metal wire inside the open laser cavity in Figure 1, our technique generates HLG modes with a fixed symmetry axes for any arbitrary non-integer OAM value. Therefore, the profile mode axes are *always* aligned to the quadrant detector measurement axes which greatly simplifies the quadrant detector operation.

2.2. Characterization of non-integer OAM beams

Figure 3 shows the resulting generated HLG beams as a function of varying orientation angle α. The open laser cavity is forced to operate at the first higher order HG mode, i.e $HG_{0,1}$. The first two rows display the measured intensity profiles of (a) the incoming $HG_{0,1}$ and (b) the outgoing $HLG_{0,1|[\alpha:0^o,90^o]}$ beams at the far-field after the collimating lens. Our generated HLG beam profiles match with the calculation shown in Figure 3(c). In the calculated images, we have used a color map to indicate the phase profile of the generated HLG modes. For outgoing HLG profiles being the analytic interpolation between a HG mode and a LG mode, we observe a more flat wavefront inside the high intensity areas (note the even color tone). Inside the dark intensity areas, the phase value increases non-linearly along the azimuthal direction. The phase singularity of zero-OAM beams at $\alpha = N \times 90^o$ forms a line (most left and most right images of Figure 3(c)), whereas for integer OAM beams at $\alpha = (2N+1) \times 45^o$ it forms a vortex (the center image of Figure 3(c)), with N an integer number. Apart from the overall scaling and slight astigmatism due to imperfect alignment, the generated HLG beams are structurally stable during propagation, as shown in Figure 4.

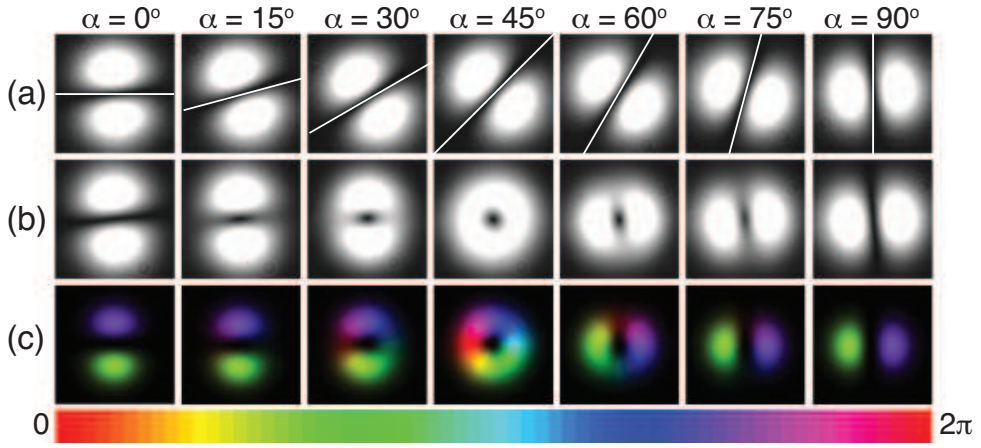

Fig. 3. [Color online] (a) Measured intensity profiles of the impinging $HG_{0,1}$ mode as a function of the orientation angle α with respect to the symmetry axes of the '$\pi/2$-mode converter'; the white lines correspond to the wire orientation in the open laser cavity of Figure 1. (b) Measured far-field intensity profiles after the collimating lens of the outgoing Hermite-Laguerre-Gauss (HLG) modes. (c) Calculated intensity profiles to compare with the measurement results in (b). The color map in the calculated intensity profiles (c) corresponds to the HLG phase profile that gradually increases from 0 to 2π.

To characterize the OAM content of the generated HLG beams, we look at the interference patterns between the outgoing HLG beam and a reference beam that comes out of the laser cavity. A typical interference pattern of an integer OAM beam shows phase dislocation features, i.e. a pitchfork that branches out into ℓ number of lines at

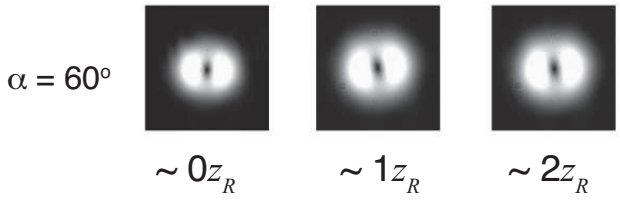

Fig. 4. Mode profiles at several Rayleigh distance z_R, representing the near- and far-field planes for the outgoing $HLG_{0,1|[\alpha:60^o]}$ mode.

the dark centre of the beam, which is also the case for the centre image of Figure 5. In the case of beams with non-integer OAM values, the branching gradually dissolves into separated shifted lines as shown by the measurement result (a) and confirmed by the calculation (b).

The perfect match between our measurement results and calculation, for both the intensity and the interference profiles, demonstrates that non-integer OAM values do indeed depend on the orientation angle of the incoming HG beam, expressed as $\ell = (n-m)\sin 2\alpha$ [25, 26]. There are two consequences of this relation when generating HLG beams using our set-up. First, the sign of ℓ changes each time α crosses the value of $N \times 90^o$. Secondly, the HLG mode profile rotates by 90^o each time α crosses the value of $(2N+1) \times 45^o$ with N an integer number. Take the example of Figure 3(b)-(c), where we have tuned the angle $0^o \leq \alpha \leq 90^o$ to obtain $0 \leq \ell \leq 1$. Although all the HLG modes shown have positive values of ℓ, the mode profiles for $\alpha \leq 45^o$ are rotated 90^o with respect to the profiles for $\alpha \geq 45^o$. Therefore, for an identical ℓ or OAM values, there are two possible orthogonal orientations of the HLG beams. The orthogonal orientation of HLG beams also greatly simplifies the calibration procedure when measuring the beam position using a quadrant detector, as will be discussed in the next section.

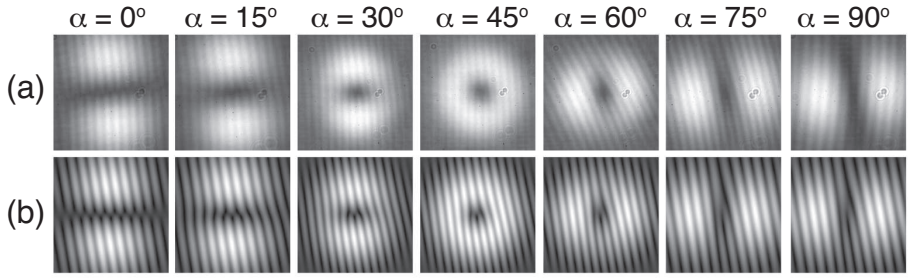

Fig. 5. The (a) measured and (b) calculated interference patterns showing the phase singularity of the HLG beams. The black color corresponds to zero intensity and zero phase, whereas the white color corresponds to maximal intensity and phase $\phi = 2\pi$.

3. Quadrant detector response to HLG beam displacement

In this section we deal with the response of a quadrant detector as a beam positional detector of HLG beams. A quadrant detector is a 2x2 array of individual p-n junction photodiodes, separated by a small gap of typically less than 0.05% of the active area, as depicted in the inset of Figure 1. The photodiodes provide the photocurrents I_{A}, I_{B}, I_{C} and I_{D} which are generated when an optical beam strikes the active area. Its position-current relation can be written as:

$$\frac{I_x}{I_\Sigma} = \frac{I_{\mathrm{A}} + I_{\mathrm{D}} - (I_{\mathrm{B}} + I_{\mathrm{C}})}{I_{\mathrm{A}} + I_{\mathrm{D}} + I_{\mathrm{B}} + I_{\mathrm{C}}} = \frac{\int_0^x \int_0^\infty |U(x,y)|^2 \,\mathrm{d}y\mathrm{d}x}{\int_0^\infty \int_0^\infty |U(x,y)|^2 \,\mathrm{d}y\mathrm{d}x}, \tag{1a}$$

$$\frac{I_y}{I_\Sigma} = \frac{I_{\mathrm{A}} + I_{\mathrm{B}} - (I_{\mathrm{C}} + I_{\mathrm{D}})}{I_{\mathrm{A}} + I_{\mathrm{B}} + I_{\mathrm{C}} + I_{\mathrm{D}}} = \frac{\int_0^y \int_0^\infty |U(x,y)|^2 \,\mathrm{d}x\mathrm{d}y}{\int_0^\infty \int_0^\infty |U(x,y)|^2 \,\mathrm{d}y\mathrm{d}x}, \tag{1b}$$

for shifts along the $x-$ and $y-$axis, respectively, with $|U(x,y)|^2$ the intensity of the impinging beam. To obtain the nominal beam displacement, the quadrant detector signal $I_{x,y}/I_\Sigma$ has to be normalized to the slope of this relationship curve, i.e. the calibration constant K.

Typically, positional beam measurements using a quadrant detector involve a fundamental Gaussian mode profile that is cylindrically symmetric, i.e. having an isotropic profile in the cylindrical coordinate system. In that case, the quadrant detector response is most sensitive around the beam center for a small displacement $\Delta x \ll w$, and the calibration constant K is derived around the beam center where the slope of positional-current relationship is linear. Previously, the quadrant detector calibration constant for LG beams as a function of ℓ has also been derived for small displacements around the beam center [30], which is valid since LG beams have also isotropic intensity profiles. For the case of HLG beams, however, one can immediately sees from Figure 3 that the intensity profile is not cylindrically symmetric. In other words, HLG beams carrying non-integer OAM have anisotropic profiles. As will be discussed in the next paragraphs, there are two things to note when operating a quadrant detector for position measurement of anisotropic beams such as HLG beams.

First, the orientation of the HLG beam profile influences the quadrant detector response. Due to the rectangular geometry of a quadrant detector, it is most natural to align the symmetry axes of the beam with respect to the quadrant detector displacement axes, as in the case of Figure 3. When these axes are aligned, the quadrant detector calibration constant K for the displacement along the $x-$axis of $\mathrm{HLG}_{n,m|\alpha}$ mode is also valid for the displacement along the $y-$axis of $\mathrm{HLG}_{m,n|\alpha}$ mode.

Second, operating a quadrant detector around the HLG beam center to detect small displacement $\Delta x \ll w$ will not always give the most sensitive position measurement. This is due to the fact that for some cases, the profile cross section $|U(x,y)|^2$ of the HLG modes along the axis of displacement, has near zero values across one displacement axis. As an example, let us observe HLG modes for $\alpha > 45^{\mathrm{o}}$ in Figure 3 (b). The low intensity values at the beam centre across the y-axis is certainly the least sensitive area to measure beam displacement along the $x-$axis. Interchangeably, the quadrant

detector is least sensitive for beam displacement along the $y-$axis around the centre area of HLG modes for $\alpha < 45^{o}$. Therefore, it is important to find the region where the quadrant detector can operate with the highest sensitivity.

3.1. Analytical solutions of quadrant detector calibration

Now, we derive the analytical expression for the position-current relationship of a quadrant detector for HLG beams carrying non-integer OAM when both of the symmetry axes overlap. This expression can be easily extended for an arbitrarily high order $\mathrm{HLG}_{n,m|\alpha}$ mode. For didactic purposes, we take the example of a radial mode index $p = 0$ and an azimuthal mode index $\ell = 1$ (i.e. $\mathrm{HLG}_{0,1|\alpha}$), and investigate the quadrant response for the beam displacement along the $x-$axis. By applying the distribution function of $\mathrm{HLG}_{0,1|\alpha}$ given in Ref. [25] into Equation (1a), we can write the x-axis displacement relationship normalized to the beam radius w for $\mathrm{HLG}_{0,1|\alpha}$ to be

$$\frac{I_x}{I_\Sigma} = -\frac{2\sqrt{2}x}{\sqrt{\pi}w}\exp\left[-2\left(\frac{x}{w}\right)^2\right]\cos^2(\alpha) + \mathrm{erf}\left(\sqrt{2}\frac{x}{w}\right). \tag{2}$$

Note that due to the symmetry axes, the same expression is found for the beam displacement of $\mathrm{HLG}_{1,0|\alpha}$ mode along the y-axis, substituting the index x with y.

We present the 1-D cross section profile in Figure 6 (a) to help visualizing the general intensity distribution of $\mathrm{HLG}_{0,1|\alpha}$ beams. The position-current relationship curves in Figure 6 (b) reveal that there are different linear regions with a constant slope (calibration constant K) for different values of α. The linear region shifts to a higher x/w value for $\alpha > 45^{o}$, coinciding with the peak intensity cross section along the displacement axis, at around $x/w = 0.7$. For $\alpha < 45^{o}$ the beam cross-section along the x-axis resembles that of a Gaussian profile and the range of linearity is around the beam center.

To confirm our analytical expression, we measure the quadrant detector response for $\mathrm{HLG}_{0,1|\alpha}$ modes, where we have used a quadrant detector from NewFocus model 2921 with an active area of 10mm $\times$ 10mm. Figure 6 (b) shows the the match between our data (open circles and dots) and the analytical solution (solid and dashed lines). It is important to realize that there exists two values of α for each $\mathrm{HLG}_{n,m|\alpha}$ mode that give the same ℓ values but with orthogonally oriented spatial distribution. These orthogonally oriented modes have different calibration constants K, as plotted in Figure 7.

To use a quadrant detector for displacement measurement of non-integer OAM beams having anisotropic profile distributions, such as HLG beams, one must pay attention to the linear range of the position-current relations, i.e. at the peak of the intensity cross section along the axis of displacement. Since the orientation of our generated HLG beam are aligned with the symmetry axes of a quadrant detector, we can easily obtain the linear range and the calibration constant K. This calibration procedure is particularly relevant for potential applications using HLG modes as non-integer OAM beams: in beam shifts measurements, high precision metrology, optical manipulation using tweezers or scanning near-field optical microscopy.

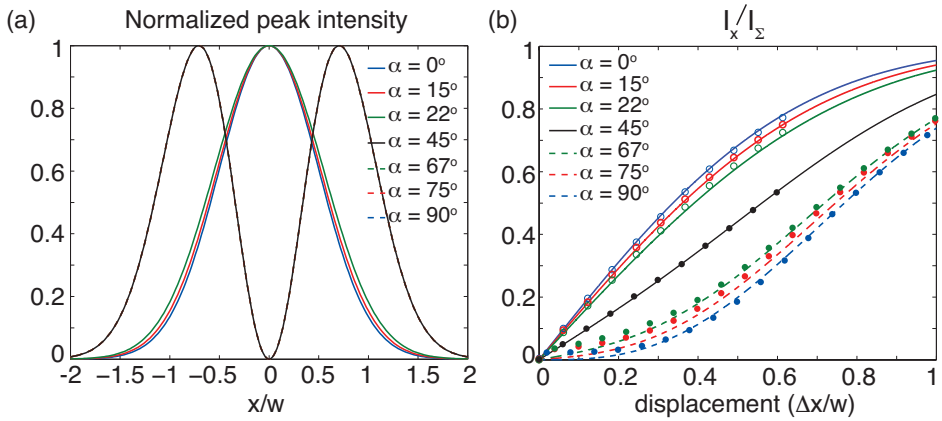

Fig. 6. (a) The cross section of the $\mathrm{HLG}_{0,1|\alpha}$ mode profile along the x-axis. (b) The corresponding response of a quadrant detector for beam displacement along the $x-$axis. Lines (both solid and dashed) and data points correspond to the analytical solution and experimental data, respectively.

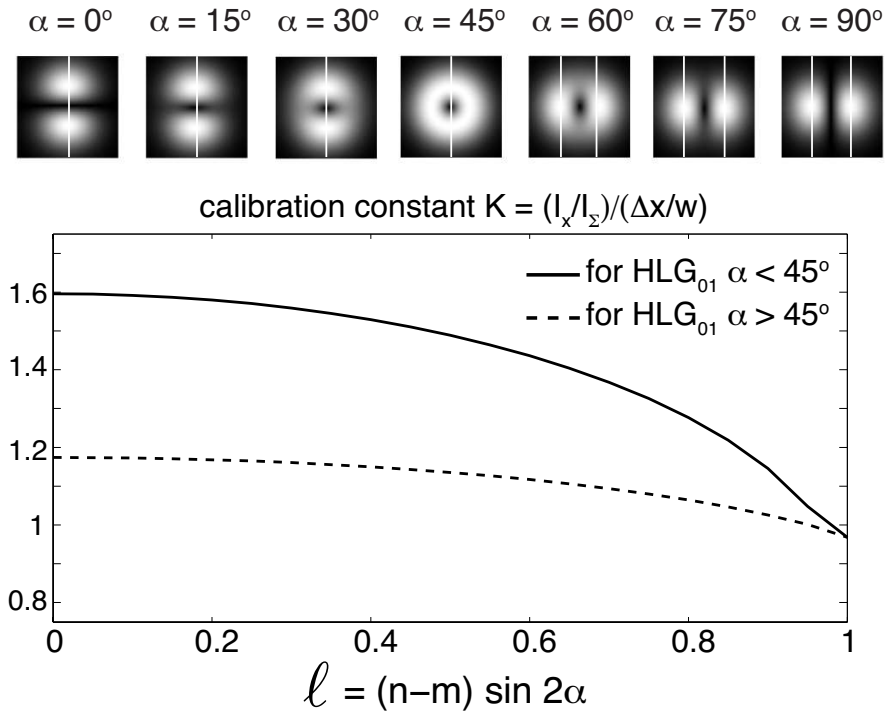

Fig. 7. The calibration constant K as a function of non-integer OAM ℓ is derived analytically for $\mathrm{HLG}_{0,1}$ modes with varying α. The white lines on the top row images illustrate the x-positions at which K is derived for several α values.

4. Conclusion

In this paper, we demonstrate a technique to generate HLG modes as non-integer OAM beams that are structurally propagation invariant and having a fixed symmetry axes for arbitrary non-integer OAM values. The experimentally demonstrated HLG beams agree with the calculation, both for the intensity profile distribution and the phase features measured with interferometric set-up.

Unlike an integer OAM beam, the phase of a HLG mode increases non-linearly along the azimuthal axis. Note that any integer OAM beam can be created from an arbitrarily higher order HLG mode having the appropriate orientation angle α. For example, $\ell = 1$ can be constructed from $\mathrm{HLG}_{0,2|[\alpha:15^o]}$, which actually produces a phase distribution that is different from that of a $\mathrm{LG}_{0,1}$ mode. In applications such as OAM beams shifts or optical manipulation using OAM beams, noticeable differences will occur when addressing an integer OAM value by using either LG modes or HLG modes.

For many applications using OAM beams, it is of high interest to measure accurately the beam position. Down to nanometer precision of beam displacement is typically measured using a quadrant detector. Different from previous techniques, the symmetry axes of our generated non-integer OAM beams are *always* aligned to the axes of quadrant detectors; which simplifies the operation and calibration of the detector.

We have derived the analytical expression and demonstrate experimentally the response of a quadrant detector towards the generated HLG beams. The obtained calibration constant *K* of a quadrant detector for HLG beams agrees with Ref. [30] only at integer ℓ, where the beam profile is isotropic or cylindrically symmetric. The assumption that a quadrant detector is most sensitive at the beam center does not always hold for general astigmatic modes, i.e. HLG modes, that has an anisotropic beam profiles.

In conclusion, we have shown that both the ℓ values and the HLG mode orientation play a role in the quadrant detector response. Furthermore, the anisotropic nature of HLG beams creates different regions having linear response of a quadrant detector when measuring beam positional shift. The beam positional measurement is most sensitive around the peak of the HLG mode profile. Our result can easily be extended to arbitrarily higher order HLG beams as solutions of light carrying higher order non-integer OAM.

Acknowledgement

This work is supported by the European Union within FET Open-FP7 ICT as part of STREP Program 255914 Phorbitech.

Bibliography

[1] L. Allen, M. W. Beijersbergen, R. J. C. Spreeuw, and J. P. Woerdman, "Orbital angular momentum of light and the transformation of Laguerre-Gaussian laser modes," Phys. Rev. A **45**, 8185–8189 (1992).

[2] E. Abramochkin and V. Volostnikov, "Beam transformation and nontransformed beams," Opt. Commun. **83**, 123–125 (1991).

[3] H. He, N. R. Heckenberg, and H. Rubinsztein-Dunlop, "Optical particle trapping with higher-order doughnut beams produced using high efficiency computer generated holograms," J. Mod. Opt. **42**, 217–223 (1995).

[4] M. Padgett and R. Bowman, "Tweezers with a twist," Nat. Photon **5**, 343–348 (2011).

[5] S. S. R. Oemrawsingh, X. Ma, D. Voigt, A. Aiello, E. R. Eliel, G. W. 'tHooft, and J. P. Woerdman, "Experimental demonstration of fractional orbital angular momentum entanglement of two photons," Phys. Rev. Lett. **95**, 240501 (2005).

[6] B. J. Pors, F. Miatto, G. W. 't Hooft, E. R. Eliel, and J. P. Woerdman, "High-dimensional entanglement with orbital-angular-momentum states of light," J. Opt. **13** (2011).

[7] G. C. G. Berkhout and M. Beijersbergen, "Measuring optical vortices in a speckle pattern using a multi-pinhole interferometer," Opt. Express **18** (2010).

[8] F. Tamburini, B. Thidé, G. Molina-Terriza, and G. Anzolin, "Twisting of light around rotating black holes," Nat. Phys. **7**, 195–197 (2011).

[9] M. Merano, N. Hermosa, J. P. Woerdman, and A. Aiello, "How orbital angular momentum affects beam shifts in optical reflection," Phys. Rev. A **82** (2010).

[10] E. G. Abramochkin and V. G. Volostnikov, "Generalized Gaussian beams," J. Opt. A: Pure Appl. Opt. **6**, S157–S161 (2004).

[11] J. Visser and G. Nienhuis, "Orbital angular momentum of general astigmatic modes," Phys. Rev. A **70**, 013809 (2004).

[12] E. G. Abramochkin, E. Razueva, and V. G. Volostnikov, "General astigmatic transform of Hermite-Laguerre-Gaussian beams," J. Opt. Soc. Am. A **27**, 2506–2513 (2010).

[13] M. W. Beijersbergen, L. Allen, H. E. L. O. van der Veen, and J. P. Woerdman, "Astigmatic laser mode converters and transfer of orbital angular momentum," Opt. Commun. **96**, 123–132 (1993).

[14] M. W. Beijersbergen, R. P. C. Coerwinkel, M. Kristensen, and J. P. Woerdman, "Helical-wavefront laser beams produced with a spiral phaseplate," Opt. Commun. **112**, 321–327 (1994).

[15] G. A. Turnbull, D. A. Robertson, G. M. Smith, L. Allen, and M. J. Padgett, "The generation of free-space Laguerre-Gaussian modes at millimetre-wave frequencies by use of a spiral phaseplate," Opt. Commun. **127**, 183–188 (1995).

[16] M. V. Berry, "Optical vortices evolving from helicoidal integer and fractional phase steps," J. Opt. A: Pure Appl. Opt. **6**, 259–268 (2004).

[17] J. Arlt, K. Dholakia, L. Allen, and M. J. Padgett, "The production of multiringed Laguerre-Gaussian modes by computer-generated holograms," J. Mod. Opt. **45**, 1231–1237 (1998).

[18] A. T. O'Neil and J. Courtial, "Mode transformations in terms of the constituent Hermite-Gaussian or LaguerreGaussian modes and the variable-phase mode converter," Opt. Commun. **181**, 35–45 (2000).

[19] E. J. Lee, Y. Park, C. S. Kim, and T. Kouh, "Detection sensitivity of the optical beam deflection method characterized with the optical spot size on the detector," Curr. Appl. Phys. **10**, 834–837 (2010).

[20] S. Cui and Y. C. Soh, "Improved measurement accuracy of the quadrant detector through improvement of linearity index," Appl. Phys. Lett. **96** (2010).

[21] Y. Panduputra, T. W. Ng, A. Neild, and M. Robinson, "Intensity influence on Gaussian beam laser based measurements using quadrant photodiodes," Appl. Opt. **49** (2010).

[22] N. Hermosa, A. Aiello, and J. P. Woerdman, "Quadrant detector calibration for vortex beams," Opt. Lett. **36** (2011).

[23] J. Woerdman, "Laser physics, fifth edition," (1995).

[24] H. Kogelink and T. Li, "Laser beams and resonators," Applied Optics **5** (1966).

[25] See: http://en.wikipedia.org/wiki/Gaussian_beam#Beam_Parameters for the figure.

[26] See for the user manual of the Newport ESP300 motion controller: http://assets.newport.com/webDocuments-EN/images/14293.PDF.

[27] See for the user manual of the Newport quadcell photoreceiver model 2901: http://assets.newport.com/webDocuments-EN/images/15194.pdf.

[28] See for the user manual of the Newport quadcell photoreceiver model 2921: http://assets.newport.com/webDocuments-EN/images/15195.pdf.